AIMS Mathematics, 11(11): 38492–38523.
DOI: 10.3934/math.20261486
Received: 10 August 2026
Revised: 15 October 2026
Accepted: 26 October 2026
Published: 19 November 2026

https://www.aimspress.com/journal/Math

Research article

Heat transfer efficiency of hybrid nanofluid over a stretching surface in porous medium with nanoparticle aggregation: finite element and response surface analyses

Jeremy Rymbai[1], **Rajesh Sharma**[1] **and Anuar Ishak**[2,*]

[1] Department of Mathematics, North-Eastern Hill University, Umshing Mawkynroh, Shillong, 793022, Meghalaya, India

[2] Department of Mathematical Sciences, Faculty of Science and Technology, Universiti Kebangsaan Malaysia, 43600 UKM Bangi, Selangor, Malaysia

* **Correspondence:** Email: anuar_mi@ukm.edu.my.

Abstract: In this study, we investigated the behavior of a hybrid nanofluid comprising of titania (TiO_2) and alumina (Al_2O_3) nanoparticles dispersed in ethylene glycol (EG), considering the effects of nanoparticle aggregation. The flow was studied over a stretching surface wihtin a porous medium, with the effects of an applied magnetic field and viscous dissipation taken into account. Modified extensions of the Krieger-Dougherty model for effective viscosity and the Maxwell and Bruggeman models for thermal conductivity were proposed to describe the hybrid nanofluid in the presence of nanoparticle aggregation. The finite element method (FEM) was employed to obtain numerical solutions of the transformed equations and the results are presented graphically. Response surface methodology (RSM) was then used to examine the effects and interactions of three key input parameters, namely the total nanoparticle volume fraction, porosity parameter, and magnetic parameter, on the local Nusselt numeber for aggregation and non-aggregation cases. In addition, sensitivity analysis was performed to quantify the influence of these parameters on the heat transfer response and to identify the parameters with greater sensitivity. The results showed that increasing the nanoparticle volume fraction and porosity parameter enhances the heat transfer rate in the presence of nanoparticle aggregation, whereas the magnetic parameter exhibits comparatively lower sensitivity within the considered range. The findings provide useful insights for thermal management and solar thermal systems, where enhanced heat transfer and optimized operating conditions are important.

Keywords: hybrid TiO_2-Al_2O_3/EG nanofluid; nanoparticle aggregation; finite element method; response surface methodology; sensitivity analysis
Mathematics Subject Classification: 62K20, 76D05, 76M10, 80A19

Nomenclature	
A_1	Positive dimensional constant
ε	Porosity
μ	Dynamic viscosity ($kg \cdot m^{-1}s^{-1}$)
u_e, u_w	Free stream and surface velocities ($m \cdot s^{-1}$)
v_w	Mass transfer velocity
ν	Kinematic viscosity ($m^2 s^{-1}$)
T, T_∞	Temperature and ambient temperature (K)
ρ	Density ($kg \cdot m^{-3}$)
ϕ_1, ϕ_2	Volume fractions of TiO_2 and Al_2O_3 nanoparticles
ϕ	Total nanoparticle volume fraction
ϕ_a	Effective volume fraction of aggregates
C_p	Specific heat capacity ($J \cdot kg^{-1}K^{-1}$)
D	Fractal index
k	Thermal conductivity ($W \cdot m^{-1}K^{-1}$)
u, v	Velocity components in x and y directions (ms^{-1})
r_p	Nanoparticle radius (m)
r_a	Aggregate radius (m)
ϕ_m, ϕ_{in}	Maximum and aggregate solid volume fractions
B_0	Magnetic field strength (T)
k_p	Permeability of porous medium (m^2)
σ	Electrical conductivity ($S \cdot m^{-1}$)
$[\zeta]$	Einstein coefficient
A	Velocity ratio parameter
Pr	Prandtl number
Ec	Eckert number
s	Injection parameter
Γ, M	Porosity and magnetic parameters
f	Dimensionless stream function
θ	Dimensionless temperature
Nu_x^*	Local Nusselt number
ψ_1, ψ_2	Shape functions
η, ψ	Similarity variable and stream function
Subscripts	
f	Base fluid
nf	Nanofluid
hnf	Hybrid nanofluid
n_1, n_2	TiO_2 and Al_2O_3 nanoparticles
$a, 1$ and $a, 2$	Aggregated TiO_2 and Al_2O_3 nanoparticles

1. Introduction

Nanofluids, owing to their improved heat transfer capabilities, are increasingly used as working fluids in fields such as manufacturing, heat dissipation in electronic systems, solar energy systems, and biomedical applications. Their superior thermal characteristics over traditional fluids have attracted considerable research interest aimed at optimising their practical applications. Hybrid nanofluids have been the focus of more recent research, which has shown that combining two types of nanoparticles often improves heat transport as compared to utilizing only one type of nanoparticle [1–3]. Hybrid nanofluids are used to improve heat transfer by increasing thermal conductivity and producing a more stable, homogeneous mixture compared to single nanoparticle dispersions. Their vast surface area and coupled nanoparticle effects aid in the formation of effective heat transfer channels. They are therefore extensively utilized in fields such as nuclear reactor cooling, machine coolants, and generator cooling. Due to its greater boiling point and lower freezing point than water, ethylene glycol (EG) is a preferred base fluid compared to water. Although EG possesses lower inherent thermal conductivity, its synergy with nanoparticles makes it a viable and often better alternative as compared to water based nanofluids. Titanium dioxide (TiO_2) has excellent dispersion behavior in EG and exhibits excellent chemical stability and low production cost [4]. Alumina (Al_2O_3) offers excellent thermal conductivity and high stability at low cost [5,6], making it a good choice for the second nanoparticle alongside TiO_2.

Magnetohydrodynamics (MHD) involves the interaction between magnetic fields and fluids capable of conducting electricity, leading to changes such as flow retardation, redirection, or stabilization. It is crucial to systems like electromagnetic pumping of molten metals, plasma control in fusion devices, and liquid-metal cooling in reactors. MHD flows are significant for numerous engineering and industrial applications since this interaction has a considerable impact on thermal transport and fluid behavior. The use of hybrid nanofluids in MHD flow systems are useful for high performance cooling, modern energy technologies, and other cutting-edge engineering applications. Zainodin et al. [7] analyzed stagnation point flow involving mixed convection in a hybrid ferrofluid subject to a magnetic field and observed that higher magnetic intensity suppresses heat transfer. They also found that while viscous dissipation further reduces heat transmission, raising the Biot number results in a notable enhancement. Bhargava et al. [8] investigated the effects of nonlinear thermal radiation and Joule heating on MHD mixed convection in a hybrid nanofluid. Their results demonstrated that buoyancy increases the fluid's primary velocity while lowering the thermal and concentration profiles. Vishalakshi et al. [9] analyzed the flow and thermal characteristics of an incompressible hybrid nanofluid over a stretching surface considering an inclined magnetic field. Yusuf et al. [10] investigated the MHD flow of a ternary hybrid nanofluid over a curved catalytic surface embedded in a porous medium, incorporating Beavers-Joseph slip and volumetric and surface non thermal heating. Their study further demonstrated the relevance of magnetic effects in controlling the transport characteristics of hybrid nanofluids in porous media. Numerous other researchers have also investigated MHD flows of different nanofluids under different physical settings and flow geometries [11–13].

Porous media, composed of interconnected pores through which fluids can pass, plays a significant role in engineering and industrial processes. It is widely used in areas like tissue engineering, air-conditioning systems, phase-change materials, material processing, solar energy devices, drug delivery, and other geophysical applications. Abderrahmane et al. [14] studied convection-driven thermal transport in a porous enclosure containing a rotating cylinder and identified combinations

of rotation speed, Hartmann number, and Darcy number that enhance heat transfer. Saghir and Rahman [15] investigated forced convection in a porous medium using several hybrid nanofluids prepared with a water-EG mixture as the base fluid, and compared their heat transfer performance. They concluded that ND-Fe_3O_4 suspended in a water-EG mixture exhibited the best heat transfer performance. Hazarika et al. [16] analyzed unsteady MHD flow of a hybrid nanofluid containing TiO_2 and Al_2O_3 nanoparticles suspended in EG within a porous medium confined between vertical plates, incorporating heat source effects and velocity constraints. Oladetan et al. [17] investigated the thermal transport and fluid flow characteristics in a microchannel heat sink using Al_2O_3-Cu/water nanofluid embedded in a porous substrate. They concluded that the hybrid nanofluid led to improved thermal performance within the channel. Several researchers have also investigated the flow and heat transfer characteristics of different fluids in porous media [18–20]. As many conventional models oversimplify the energy loss in extremely permeable structures, it is challenging to capture viscous dissipation in porous media. To resolve this, Al-Hadhrami et al. [21] proposed a thermodynamically consistent formulation that holds true for a broad varieties of permeabilities. In this study, their model is employed to account for viscous dissipation in TiO_2-Al_2O_3/EG nanofluid flowing within a porous medium.

Nanoparticles suspended in a fluid often interact and bind together, resulting in the formation of clusters or aggregates. These aggregates arise mainly from interparticle attractions such as van der Waals forces. Motevasel et al. [22] noted that such aggregation effects remain significant even when particle concentration is low, and therefore should not be disregarded in nanofluid modeling. A number of studies [23–25] show that the thermal transport capability of nanofluids is strengthened when nanoparticle aggregation effects is considered. Chen et al. [26] introduced a validated model for TiO_2/EG nanofluid that accounts for the impact of nanoparticle aggregation. In their formulation, a modified Krieger-Dougherty relation describes the change in viscosity caused by aggregation, while modified Maxwell and Bruggeman models capture the thermal conductivity. This framework has been used in a number of studies [27–29] to analyze TiO_2/EG nanofluids while taking aggregation effects into account under different flow configurations and physical conditions. Studies reveal that the influence of nanoparticle aggregation in hybrid nanofluids has not been examined when a secondary nanoparticle other than TiO_2 is introduced.

Several researchers have investigated the use of nanofluids as heat transfer fluids in solar collectors, owing to their potential to improve the thermal performance of these systems. Nanofluids have been examined in different types of solar thermal collectors, including flat plate, evacuated tube, and concentrating collectors, with improvements in heat transfer and thermal efficiency reported under suitable operating conditions [30–32]. Moreover, attention has also been directed toward hybrid nanofluids for solar thermal applications, as the combination of different nanoparticles can provide enhanced thermal and optical characteristics compared with conventional fluids and mono-nanofluids [33–35]. However, nanoparticle stability and aggregation remain important considerations in the practical application of hybrid nanofluids in solar thermal systems, as aggregate formulation can alter the thermophysical and optical properties of the working fluid and consequently affect the thermal performance of solar collectors. Despite this, the effects of nanoparticle aggregation are not explicitly considered in many studies of nanofluid based solar thermal systems, highlighting the need for further investigation of aggregation effects when evaluating the heat transfer performance of hybrid nanofluids.

Despite the growing use of hybrid nanofluids in MHD and porous medium heat transfer systems, nanoparticle aggregation has primarily been considered in mono-nanofluids. In particular, nanoparticle aggregation has not been incorporated into hybrid nanofluid models, creating a need to extend aggregation formulations beyond mono-nanofluids and investigate its influence on hybrid nanofluid heat transfer. To address this gap, we develop a model for TiO_2-Al_2O_3/EG hybrid nanofluid over a stretching surface in a porous medium, incorporating nanoparticle aggregation together with magnetic and viscous dissipation effects. Modified expressions for the effective viscosity and thermal conductivity are formulated to account for the presence of aggregates in the hybrid nanofluid. Furthermore, response surface methodology (RSM) is employed to investigate the individual and interactive effects of the governing parameters and to determine the conditions corresponding to enhanced heat transfer. Sensitivity analysis is subsequently performed to quantify the influence of the selected parameters on the heat transfer response. The combined consideration of hybrid nanoparticle aggregation, heat transfer optimization, and parameter sensitivity provides a broader assessment of the thermal behavior of hybrid nanofluids and constitutes the main contribution of this study.

2. Mathematical formulation

MHD stagnation point flow of TiO_2-Al_2O_3/EG nanofluid over a stretching surface within a porous medium, considering viscous dissipation and nanoparticle aggregation, is being examined. To represent the impact of aggregation, modified extensions of the Krieger-Dougherty model for effective viscosity and the Maxwell-Bruggeman formulations for thermal conductivity are proposed, which are adapted to the hybrid nanofluid. Figure 1 depicts the physical configuration of this study.

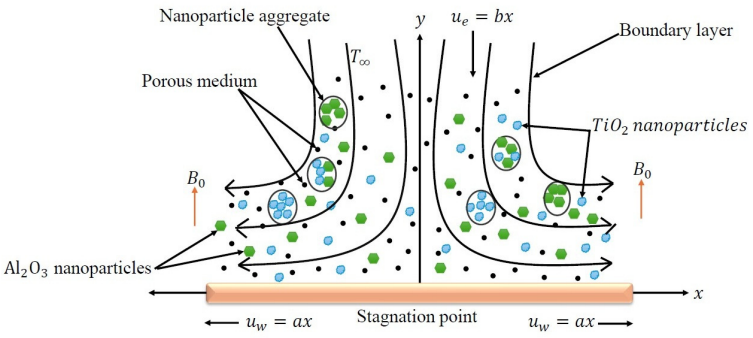


Figure 1. Representation of the physical system

The governing mathematical model is then formulated under the following assumptions:

- The fluid motion is assumed to be steady, laminar, and incompressible.
- The surface velocity is assumed to be $u_w = ax$, while the free stream velocity is taken as $u_e = bx$.
- The far field temperature T_∞ is maintained at a constant value, while the wall temperature is assumed as $T_w = T_\infty + A_1 x^2$, with A_1 denoting a positive dimensional parameter.
- Al-Hadhrami formulation [21] is used for viscous dissipation in porous media.
- Nanoparticle aggregation is considered, where the formation of particle clusters is driven by interparticle forces, particularly the van der Waals attraction.

- The induced magnetic field generated by the fluid motion is assumed to be negligible and only the externally applied magnetic field is considered in the analysis.
- The effect of the magnetic field on the electrostatic properties of nanoparticle aggregates is neglected in this analysis.
- It is assumed that the aggregates may be formed from TiO_2 particles, Al_2O_3, or combinations of the two, and that these aggregate types coexist in the suspension.
- Any interaction between the aggregates occurs only through their combined contribution to the effective thermophysical properties of the nanofluid (as summarized in Table 1).
- Aggregates are assumed to follow diffusion-limited cluster aggregates (DLCA) in EG.
- The values of $\frac{r_a}{r_p}$, D, ϕ_m and $[\zeta]$ are taken from the experimental observations of Chen et al. [26] and are given as follows: $\dfrac{r_a}{r_p} = 3.34$, $D = 1.8$, $\phi_m = 0.605$, and $[\zeta] = 2.5$. Since experimental aggregation data and corresponding fractal parameters for Al_2O_3/EG are not considered in the formulation, the same parameters are assumed for both TiO_2 and Al_2O_3 aggregates. This assumption provides a consistent basis for extending the aggregation model of Chen et al. [26] from a mono-nanofluid to the TiO_2-Al_2O_3/EG hybrid nanofluid. The use of these parameters for Al_2O_3 is therefore considered a modeling approximation, and experimental data for Al_2O_3/EG would be valuable for further refinement of this model.

Table 1. Nanofluid thermophysical properties with and without nanoparticle aggregation.

Effective property	**Without aggregation**	**With aggregation**
Density	$\rho_{hnf} = (1-\phi_2)[(1-\phi_1)\rho_f + \phi_1\rho_{n_1}] + \phi_2\rho_{n_2}$	$\rho_{hnf} = (1-\phi_{a,2})[(1-\phi_{a,1})\rho_f + \phi_{a,1}\rho_{n_1}] + \phi_{a,2}\rho_{n_2}$
Dynamic viscosity	$\dfrac{\mu_{hnf}}{\mu_f} = \dfrac{1}{(1-\phi_1)^{2.5}(1-\phi_2)^{2.5}}$	$\dfrac{\mu_{hnf}}{\mu_f} = \left(1 - \dfrac{\phi_a}{\phi_m}\right)^{[\zeta]\phi_m}$
Specific heat capacity	$\dfrac{(\rho C_p)_{hnf}}{(\rho C_p)_f} = (1-\phi_2)\left[(1-\phi_1)+\phi_1\dfrac{(\rho C_p)_{n_1}}{(\rho C_p)_f}\right]+\phi_2\dfrac{(\rho C_p)_{n_2}}{(\rho C_p)_f}$	$\dfrac{(\rho C_p)_{hnf}}{(\rho C_p)_f} = (1-\phi_{a,2})\left[(1-\phi_{a,1}) + \phi_{a,1}\dfrac{(\rho C_p)_{n_1}}{(\rho C_p)_f}\right] + \phi_{a,2}\dfrac{(\rho C_p)_{n_2}}{(\rho C_p)_f}$
Electrical conductivity	$\sigma_{nf} = \sigma_f \times \left(\dfrac{\sigma_{n_1} + 2\sigma_f - 2\phi_1(\sigma_f - \sigma_{n_1})}{\sigma_{n_1} + 2\sigma_f + \phi_1(\sigma_f - \sigma_{n_1})}\right)$	$\sigma_{nf} = \sigma_f \times \left(\dfrac{\sigma_{n_1} + 2\sigma_f - 2\phi_{a,1}(\sigma_f - \sigma_{n_1})}{\sigma_{n_1} + 2\sigma_f + \phi_{a,1}(\sigma_f - \sigma_{n_1})}\right)$
	$\sigma_{hnf} = \sigma_{nf} \times \left(\dfrac{\sigma_{n_2} + 2\sigma_{nf} - 2\phi_2(\sigma_{nf} - \sigma_{n_2})}{\sigma_{n_2} + 2\sigma_{nf} + \phi_2(\sigma_{nf} - \sigma_{n_2})}\right)$	$\sigma_{hnf} = \sigma_{nf} \times \left(\dfrac{\sigma_{n_2} + 2\sigma_{nf} - 2\phi_{a,2}(\sigma_{nf} - \sigma_{n_2})}{\sigma_{n_2} + 2\sigma_{nf} + \phi_{a,2}(\sigma_{nf} - \sigma_{n_2})}\right)$
Thermal conductivity	$k_{nf} = k_f \times \left(\dfrac{k_{n_1} + 2k_f - 2\phi_1(k_f - k_{n_1})}{k_{n_1} + 2k_f + \phi_1(k_f - k_{n_1})}\right)$	$k_{nf} = k_f \times \left(\dfrac{k_{a,1} + 2k_f - 2\phi_{a,1}(k_f - k_{a,1})}{k_{a,1} + 2k_f + \phi_{a,1}(k_f - k_{a,1})}\right)$
	$k_{hnf} = k_{nf} \times \left(\dfrac{k_{n_2} + 2k_{nf} - 2\phi_2(k_{nf} - k_{n_2})}{k_{n_2} + 2k_{nf} + \phi_2(k_{nf} - k_{n_2})}\right)$	$k_{hnf} = k_{nf} \times \left(\dfrac{k_{a,2} + 2k_{nf} - 2\phi_{a,2}(k_{nf} - k_{a,2})}{k_{a,2} + 2k_{nf} + \phi_{a,2}(k_{nf} - k_{a,2})}\right)$

With these assumptions, the governing equations of the flow can be written as

$$\frac{\partial u}{\partial x} + \frac{\partial v}{\partial y} = 0, \tag{2.1}$$

$$u\frac{\partial u}{\partial x} + v\frac{\partial u}{\partial y} = u_e\frac{du_e}{dx} + \nu_{hnf}\frac{\partial^2 u}{\partial y^2} + \frac{\sigma_{hnf}}{\rho_{hnf}}B_0^2(u_e - u) - \nu_{hnf}\frac{\varepsilon u}{k_p}, \tag{2.2}$$

$$u\frac{\partial T}{\partial x} + v\frac{\partial T}{\partial y} = \frac{k_{hnf}}{(\rho C_p)_{hnf}}\frac{\partial^2 T}{\partial y^2} + \frac{\nu_{hnf}\varepsilon}{(C_p)_{hnf}k_p}u^2 + \frac{\nu_{hnf}}{(C_p)_{hnf}}\left(\frac{\partial u}{\partial y}\right)^2. \tag{2.3}$$

The boundary conditions associated with the system are given as

$$u(x,0) = u_w(x), \quad v(x,0) = v_w, \quad T(x,0) = T_w, \tag{2.4}$$

$$u(x,\infty) = u_e(x), \quad T(x,\infty) = T_\infty. \tag{2.5}$$

To incorporate aggregation effects, the Krieger-Dougherty model is modified for application to hybrid nanofluid effective viscosity. The total effective volume fraction of the nanoparticle aggregates is given by

$$\phi_a = \phi_{a,1} + \phi_{a,2}, \tag{2.6}$$

where $\phi_{a,1} = \phi_1\left(\frac{r_a}{r_p}\right)^{3-D}$ and $\phi_{a,2} = \phi_2\left(\frac{r_a}{r_p}\right)^{3-D}$.

Here, $\phi_{a,1}$ and $\phi_{a,2}$ represent the effective volume contributions of the aggregates associated with TiO_2 and Al_2O_3, respectively. Their sum, ϕ_a, therefore represents the total effective volume fraction of the aggregate population in the hybrid nanofluid. The formulation enables TiO_2, Al_2O_3, and mixed aggregates to coexist, but does not explicitly distinguish the composition of individual mixed aggregates.

An expression for the thermal conductivities of the aggregates are given by

$$k_{a,i} = \frac{k_f}{4}\left[(3\phi_{in} - 1)\frac{k_{n_i}}{k_f} + (3(1-\phi_{in}) - 1) + \left\{\left((3\phi_{in} - 1)\frac{k_{n_i}}{k_f} + (3(1-\phi_{in}) - 1)\right)^2 + 8\frac{k_{n_i}}{k_f}\right\}^{\frac{1}{2}}\right], \tag{2.7}$$

where k_{n_i}, for $i = 1, 2$ are the thermal conductivities of the two nanoparticles and $\phi_{in} = \left(\frac{r_a}{r_p}\right)^{D-3}$.

The main relationships utilized to assess the nanofluid characteristics are summarized in Table 1. Table 2 lists the thermal and material characteristics of EG, TiO_2, and Al_2O_3 used in this study.

Table 2. Thermal and material characteristics of the base fluid and nanoparticles.

	ρ (kg/m^3)	C_p (J/kgK)	k (W/mK)	σ (S/m)
EG	1114	2415	0.252	5.5×10^{-6}
TiO_2	4250	686.2	8.9538	2.38×10^{6}
Al_2O_3	3970	765	40	10^{-12}

3. Numerical method

The transformation variables given below enable the reduction of Eqs (2.2) and (2.3) into coupled ordinary differential equations (ODEs):

$$u = axf'(\eta), \quad v = -\sqrt{a\nu_f}f(\eta), \quad \eta = \sqrt{\frac{a}{\nu_f}}y, \quad \theta(\eta) = \frac{T - T_\infty}{T_w - T_\infty},$$

where f and θ represent the dimensionless stream function and temperature, respectively. The transformed equations are given below:

$$\left(\frac{\mathbb{A}_1}{\mathbb{A}_2}\right)f''' + ff'' - f'^2 + \left(\frac{\mathbb{A}_3}{\mathbb{A}_2}\right)M(A - f') - \left(\frac{\mathbb{A}_1}{\mathbb{A}_2}\right)\Gamma f' + A^2 = 0, \tag{3.1}$$

$$\mathbb{A}_5\theta'' + \mathbb{A}_4 Pr(f\theta' - 2f'\theta) + \mathbb{A}_1 Pr \cdot Ec(\Gamma f'^2 + f''^2) = 0, \tag{3.2}$$

where

$$\mathbb{A}_1 = \frac{\mu_{hnf}}{\mu_f}, \ \mathbb{A}_2 = \frac{\rho_{hnf}}{\rho_f}, \ \mathbb{A}_3 = \frac{\sigma_{hnf}}{\sigma_f}, \ \mathbb{A}_4 = \frac{(\rho C_p)_{hnf}}{(\rho C_p)_f}, \ \mathbb{A}_5 = \frac{k_{hnf}}{k_f},$$

$$M = \frac{\sigma_f B_0^2}{\rho_f a} \text{ (Magnetic parameter)}, \ \Gamma = \frac{\varepsilon\nu_f}{k_p a} \text{ (Porosity parameter)},$$

$$A = \frac{b}{a} \text{ (velocity ratio parameter)}, \ Pr = \frac{(\mu C_p)_f}{k_f} \text{ (Prandtl number)},$$

$$Ec = \frac{u_w^2}{(C_p)_f(T_w - T_\infty)} \text{ (Eckert number)}, \ s = -\frac{v_w}{\sqrt{a\nu_f}} \text{ (injection parameter)}.$$

The detailed expressions for the viscous dissipation terms in Eq (3.2) are provided in the Appendix. The introduction of dimensionless parameters simplifies the governing equations by reducing the number of independent variables and parameters. These parameters also provide a convenient means of characterizing the relative contributions of the different physical effects governing the flow and heat transfer. Furthermore, the dimensionless formulation facilitates the numerical treatment of the problem and enables the effects of the governing parameters to be systematically investigated and compared.

For clarity, representative substitutions of the effective thermophysical properties in Table 1 into the dimensionless coefficients used in the governing equations are given below. For example, the viscosity ratio $\mathbb{A}_1 = \frac{\mu_{hnf}}{\mu_f}$ is obtained as

$$\mathbb{A}_1 = \frac{1}{(1 - \phi_1)^{2.5}(1 - \phi_2)^{2.5}},$$

for the non-aggregation case, whereas

$$\mathbb{A}_1 = \left(1 - \frac{\phi_a}{\phi_m}\right)^{[\zeta]\phi_m},$$

when nanoparticle aggregation is considered. Similarly, since $\mathbb{A}_5 = \dfrac{k_{hnf}}{k_f}$, the sequential Maxwell model for the thermal conductivity gives

$$\mathbb{A}_5 = \frac{k_{hnf}}{k_f} = \left(\frac{k_{n_1} + 2k_f - 2\phi_1(k_f - k_{n_1})}{k_{n_1} + 2k_f + \phi_1(k_f - k_{n_1})}\right)\left(\frac{k_{n_2} + 2k_{nf} - 2\phi_2(k_{nf} - k_{n_2})}{k_{n_2} + 2k_{nf} + \phi_2(k_{nf} - k_{n_2})}\right),$$

without aggregation. When aggregation is included, the corresponding expression is

$$\mathbb{A}_5 = \frac{k_{hnf}}{k_f} = \left(\frac{k_{a,1} + 2k_f - 2\phi_{a,1}(k_f - k_{a,1})}{k_{a,1} + 2k_f + \phi_{a,1}(k_f - k_{a,1})}\right)\left(\frac{k_{a,2} + 2k_{nf} - 2\phi_{a,2}(k_{nf} - k_{a,2})}{k_{a,2} + 2k_{nf} + \phi_{a,2}(k_{nf} - k_{a,2})}\right),$$

where $k_{a,1}$ and $k_{a,2}$ are obtained from (2.7). These substitutions illustrate how the effective property relations listed in Table 1 enter the dimensionless formulation. The remaining coefficients $\mathbb{A}_2, \ldots, \mathbb{A}_4$ are obtained analogously from their respective effective property expressions in Table 1.

Since $(T_w - T_\infty) = A_1 x^2$, the dimensionless temperature definition, $\theta(\eta) = \dfrac{(T - T_\infty)}{T_w - T_\infty}$, gives the similarity form, $T(x, y) = T_\infty + A_1 x^2 \theta(\eta)$, which is consistent with the prescribed wall temperature. Consequently, the boundary conditions in (2.4) and (2.5) are transformed to

$$f(0) = s, \quad f'(0) = 1, \quad f'(\infty) = A, \tag{3.3}$$

$$\theta(0) = 1, \quad \theta(\infty) = 0. \tag{3.4}$$

The principal physical quantity of interest in this study is the Nusselt number and is given as

$$Nu_x = -\frac{k_{hnf} x \left(\frac{\partial T}{\partial y}\right)_{y=0}}{k_f(T_w - T_\infty)}.$$

Additionally, the local Nusselt number is given as

$$Nu_x^* = Re_x^{-1/2} Nu_x = -\mathbb{A}_5 \theta'(0),$$

where $Re_x = \frac{u_e(x)x}{\nu_f}$ is the local Reynolds number.

The ODEs in Eqs (3.1) and (3.2), along with the boundary condtions (3.3) and (3.4), are solved numerically using the Galerkin finite element method (FEM) [36, 37]. FEM is adopted in this study because of its flexibility in treating the nonlinear coupled boundary value problem resulting from the governing flow and energy equations. In particular, the formulation enables the nonlinear terms and variable effective thermophysical properties associated with nanoparticle aggregation to be incorporated directly into the discretized system. FEM also provides systematic control over the computational domain through mesh refinement, making it suitable for obtaining accurate solutions of the velocity and temperature fields in the current boundary layer problem. The reliability of the numerical solution is further assessed through mesh independence and convergence checks.

Despite these advantages, FEM has limitations. The accuracy of the solution depends on the quality and resolution of the computational mesh, particularly in regions where the solution exhibits strong gradients. A finer mesh may therefore be required to achieve the desired accuracy, which increases the computational cost. Additionally, the nonlinear algebraic system resulting from the discretization

requires an iterative solution procedure and convergence may depend on the initial approximation and the selected convergence criterion. These considerations should be taken into account when extending the formulation to more complex flow configurations or strongly nonlinear systems.

Figure 2 outlines the step-by-step numerical framework used in this study.

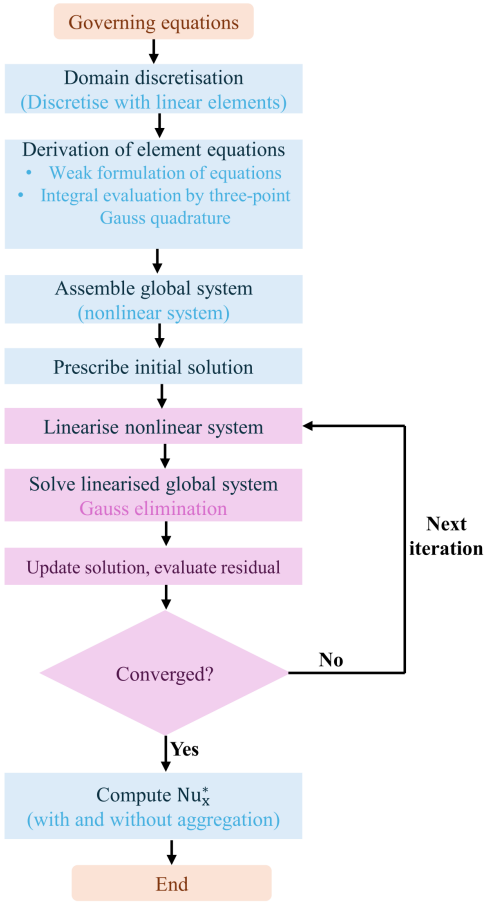


Figure 2. Flowchart of the solution methodology.

The initial step in FEM involves the following assumption:

$$f' = h. \tag{3.5}$$

Then Eqs (3.1) and (3.2) reduce to

$$\left(\frac{\mathbb{A}_1}{\mathbb{A}_2}\right)h'' + fh' - h^2 + \left(\frac{\mathbb{A}_3}{\mathbb{A}_2}\right)M(A-h) - \left(\frac{\mathbb{A}_1}{\mathbb{A}_2}\right)\Gamma h + A^2 = 0, \tag{3.6}$$

$$\mathbb{A}_5\theta'' + \mathbb{A}_4 Pr(f\theta' - 2h\theta) + \mathbb{A}_1 Pr \cdot Ec(\Gamma h^2 + h'^2) = 0. \tag{3.7}$$

The boundary conditions can be then expressed as

$$f(0) = s, \quad h(0) = 1, \quad h(\infty) = A, \tag{3.8}$$

$$\theta(0) = 1, \quad \theta(\infty) = 0. \tag{3.9}$$

On the linear element (η_e, η_{e+1}), the weak forms of Eqs (3.5)–(3.7) are given by

$$\int_{\eta_e}^{\eta_{e+1}} w_1(f' - h)d\eta = 0, \tag{3.10}$$

$$\int_{\eta_e}^{\eta_{e+1}} w_2\left[\left(\frac{\mathbb{A}_1}{\mathbb{A}_2}\right)h'' + fh' - h^2 + \left(\frac{\mathbb{A}_3}{\mathbb{A}_2}\right)M(A - h) - \left(\frac{\mathbb{A}_1}{\mathbb{A}_2}\right)\Gamma h + A^2\right] = 0, \tag{3.11}$$

$$\int_{\eta_e}^{\eta_{e+1}} w_3\left[\mathbb{A}_5\theta'' + \mathbb{A}_4 Pr(f\theta' - 2h\theta) + \mathbb{A}_1 Pr \cdot Ec(\Gamma h^2 + h'^2)\right] = 0, \tag{3.12}$$

where w_1, w_2, and w_3 denote the shape functions associated with small variations in f, h, and θ, respectively.

Let

$$f = \sum_{j=1}^{2} f_j\psi_j, \quad h = \sum_{j=1}^{2} h_j\psi_j, \quad \theta = \sum_{j=1}^{2} \theta_j\psi_j, \tag{3.13}$$

with $w_1 = w_2 = w_3 = \psi_j$ $(j = 1, 2)$. Here, $\psi_j's$ are the shape functions for each element (η_e, η_{e+1}) and are given as

$$\psi_1 = \frac{\eta_{e+1} - \eta}{\eta_{e+1} - \eta_e} \text{ and } \psi_2 = \frac{\eta - \eta_e}{\eta_{e+1} - \eta_e}, \quad \eta_e \le \eta \le \eta_{e+1}.$$

Substituting Eq (3.13) into Eqs (3.10)–(3.12) yields the following finite element formulation:

$$\begin{bmatrix}\begin{bmatrix}L^{11}\\L^{21}\\L^{31}\end{bmatrix} & \begin{bmatrix}L^{12}\\L^{22}\\L^{32}\end{bmatrix} & \begin{bmatrix}L^{13}\\L^{23}\\L^{33}\end{bmatrix}\end{bmatrix}\begin{bmatrix}f\\h\\\theta\end{bmatrix} = \begin{bmatrix}\{b^1\}\\\{b^2\}\\\{b^3\}\end{bmatrix}, \tag{3.14}$$

where $[L^{mn}], [b^m] (m, n = 1, 2, 3)$ are defined as

$$L_{ij}^{11} = \int_{\eta_e}^{\eta_{e+1}} \psi_i \frac{d\psi_j}{d\eta}d\eta, \quad L_{ij}^{12} = -\int_{\eta_e}^{\eta_{e+1}} \psi_i\psi_j d\eta, \quad L_{ij}^{13} = 0,$$

$$L_{ij}^{21} = \frac{\mathbb{A}_2}{\mathbb{A}_1}\left[\overline{h_1}\int_{\eta_e}^{\eta_{e+1}} \psi_i \frac{d\psi_1}{d\eta}\psi_j d\eta + \overline{h_2}\int_{\eta_e}^{\eta_{e+1}} \psi_i \frac{d\psi_2}{d\eta}\psi_j d\eta\right],$$

$$L_{ij}^{22} = -\int_{\eta_e}^{\eta_{e+1}} \frac{d\psi_i}{d\eta}\frac{d\psi_j}{d\eta}d\eta - \frac{\mathbb{A}_2}{\mathbb{A}_1}\left[\overline{h_1}\int_{\eta_e}^{\eta_{e+1}} \psi_i\psi_1\psi_j d\eta + \overline{h_2}\int_{\eta_e}^{\eta_{e+1}} \psi_i\psi_2\psi_j d\eta\right] - \left(\frac{\mathbb{A}_3}{\mathbb{A}_1}M + \Gamma\right)\int_{\eta_e}^{\eta_{e+1}} \psi_i\psi_j d\eta,$$

$$L_{ij}^{23} = 0, \quad L_{ij}^{31} = 0,$$

$$L_{ij}^{32} = \left(\frac{\mathbb{A}_1}{\mathbb{A}_5}\right) Pr \cdot Ec \cdot \Gamma\left[\overline{h_1}\int_{\eta_e}^{\eta_{e+1}} \psi_i\psi_1\psi_j d\eta + \overline{h_2}\int_{\eta_e}^{\eta_{e+1}} \psi_i\psi_2\psi_j d\eta\right] \tag{3.15}$$
$$+ \left(\frac{\mathbb{A}_1}{\mathbb{A}_5}\right) Pr \cdot Ec\left[\overline{h_1}\int_{\eta_e}^{\eta_{e+1}} \psi_i\frac{d\psi_1}{d\eta}\frac{d\psi_j}{d\eta} + \overline{h_2}\int_{\eta_e}^{\eta_{e+1}} \psi_i\frac{d\psi_2}{d\eta}\frac{d\psi_j}{d\eta}d\eta\right],$$

$$L_{ij}^{33} = -\int_{\eta_e}^{\eta_{e+1}} \frac{d\psi_i}{d\eta}\frac{d\psi_j}{d\eta}d\eta + \left(\frac{\mathbb{A}_4}{\mathbb{A}_5}\right)Pr\left[\overline{f_1}\int_{\eta_e}^{\eta_{e+1}} \psi_i\psi_1\frac{d\psi_j}{d\eta} + \overline{f_2}\int_{\eta_e}^{\eta_{e+1}} \psi_i\psi_2\frac{d\psi_j}{d\eta}d\eta\right] \tag{3.16}$$
$$- 2\left(\frac{\mathbb{A}_4}{\mathbb{A}_5}\right)Pr\left[\overline{h_1}\int_{\eta_e}^{\eta_{e+1}} \psi_i\psi_1\psi_j d\eta + \overline{h_2}\int_{\eta_e}^{\eta_{e+1}} \psi_i\psi_2\psi_j d\eta\right],$$

$$b_i^1 = 0, \quad b_i^2 = -\left[\psi_i\frac{d\psi_i}{d\eta}\right]_{\eta_e}^{\eta_{e+1}} - \frac{A}{\mathbb{A}_1}(\mathbb{A}_3 M + \mathbb{A}_2 A)\int_{\eta_e}^{\eta_{e+1}} \psi_i d\eta, \quad b_i^3 = -\left[\psi_i\frac{d\psi_i}{d\eta}\right]_{\eta_e}^{\eta_{e+1}}.$$

The system of Eq (3.14) is nonlinear; therefore, an iterative scheme is used to solve it. The initial guess of zero is taken at each node point. The system of equations is linearized using the Picard's iterative scheme, taking the known approximations $\overline{f_i}$ and $\overline{h_i}$ $(i = 1, 2)$, of the variables f and h. After applying the given boundary conditions, the resulting system of equations is solved using the Gauss elimination method. This solution acts as a new set of values for next iterations. This process is continued until the absolute difference between the unknowns at two successive iterations becomes less than the prescribed convergence tolerance of 10^{-8}, subject to a maximum of 1000 iterations.

3.1. Validation

After the convergence tolerance of 10^{-8} is achieved, the FEM solution is further verified through a mesh independence study, as summarized in Table 3.

Table 3. Mesh independence analysis for $|f''(0)|$ and $|\theta'(0)|$ with varying number of elements for $\phi_1 = \phi_2 = 0.05$, $A = 2$, $\Gamma = 0.1$, $Pr = 150.4583$, $Ec = 0.1$, and $M = 20$.

Number of elements	$\|f''(0)\|$	$\|\theta'(0)\|$
60	3.54289	0.52581
100	3.55899	0.48071
150	3.56431	0.46577
200	3.56623	0.46039
300	3.56762	0.45647
500	3.56835	0.45443
600	3.56847	0.45408
700	3.56855	0.45386

Since the difference in the results obtained for 600 and 700 elements is below 0.05%, the mesh consisting of 600 elements is considered sufficiently accurate and is therefore used for all further computations. Validation is carried out by comparing the computed values of $-f''(0)$ with the benchmark values reported by Pop et al. [38] and Masood et al. [39]. Table 4 compares this comparison

for different values of A with $\phi_1 = \phi_2 = s = Ec = \Gamma = M = 0$. The excellent consistency observed in the results confirms the validity of this study.

Table 4. Comparison of values of $-f''(0)$ for various values of A for $\phi_1 = \phi_2 = s = Ec = \Gamma = M = 0$.

A	Pop et al. [38]	Masood et al. [39]	Current results
0.1	0.9694	0.96939	0.969431
0.2	0.9181	0.91811	0.918109
0.5	0.6673	0.66726	0.667253

4. Results and discussion

The computational results and their related thermal and physical implications are examined in this section. The impact of the parameters A, Γ, M, s, and Ec on the velocity $f'(\eta)$ and the temperature $\theta(\eta)$ are shown and discussed. For all numerical computations, the semi-infinite computational domain is truncated at $\eta_\infty = 3$. The truncation value is selected based on preliminary numerical tests, which shows that extending the computational domain beyond $\eta_\infty = 3$ produces no significant change in the computed velocity and temperature profiles. Thus, $\eta_\infty = 3$ is considered sufficiently large to represent the far field boundary conditions while maintaining computational efficiency. For the graphical analysis of the velocity and temperature profiles, the baseline parameter values specified later in this section are selected based on the preliminary numerical testing to ensure stable and converged solutions with appropriate asymptotic behavior. These values provide suitable reference conditions for examining the individual effects of the governing parameters, while the remaining parameters are kept fixed when each parameter is varied. In the figures, solid lines correspond to cases with nanoparticle aggregation, whereas the dashed lines represent cases without aggregation.

4.1. Effect of different parameters on flow characteristics

The baseline parameter values used for the velocity profile analysis are $\phi_1 = \phi_2 = 0.05$, $A = 0.1$, $s = -1$, $\Gamma = 0.1$, $Ec = 0.1$, and $M = 20$. The influence of the velocity ratio parameter (A) on the velocity profile ($f'(\eta)$) is shown in Figure 3. An increase in A causes the velocity profile to rise systematically throughout the boundary layer. This behavior is associated with the prescribed external flow velocity, since a larger velocity ratio increases the external flow contribution relative to the stretching surface and consequently enhances the fluid velocity. In general, the velocity profile is lower when nanoparticle aggregation is considered. This difference results from the modification of the effective thermophysical properties of the hybrid nanofluid, particularly the increase in effective viscosity, which provides greater resistance to momentum transport. The effect of the porosity parameter (Γ) on $f'(\eta)$ is presented in Figure 4. As Γ increases, the velocity decreases in both cases. As Γ represents the dimensionless porous resistance parameter, defined in terms of the porosity (ε), permeability (k_p), and the reference flow quantities, an increase in Γ strengthens the porous medium resistance, thereby opposing the fluid motion and reducing the velocity. The aggregated case exhibits a lower velocity than the non-aggregated case over the considered range.

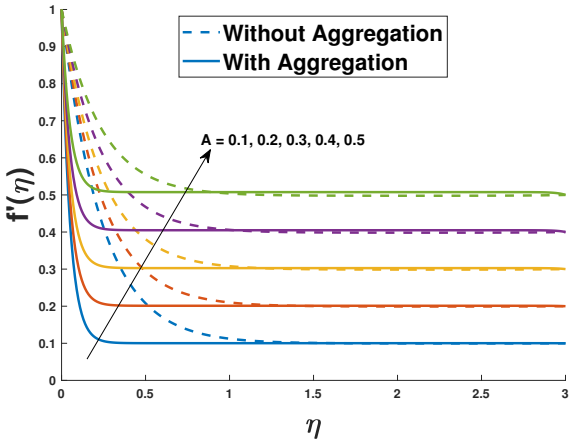


Figure 3. Effect of A on $f'(\eta)$ for $\phi_1 = \phi_2 = 0.05$, $s = -1$, $\Gamma = 0.1$, $Ec = 0.1$, and $M = 20$.

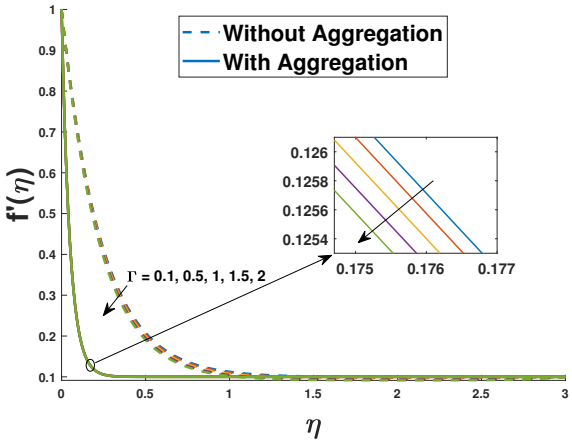


Figure 4. Effect of Γ on $f'(\eta)$ for $\phi_1 = \phi_2 = 0.05$, $A = 0.1$, $s = -1$, $Ec = 0.1$, and $M = 20$.

Figure 5 depicts the effect of the magnetic parameter (M) on the velocity profile. Increasing M reduces the velocity in both cases. This behavior results from the stronger Lorentz force generated by the applied magnetic field. As the magnetic parameter increases, the magnetic interaction becomes stronger and increasingly opposes the fluid motion, thereby suppressing the velocity within the boundary layer. The influence of aggregation remains evident through the lower velocity profile associated with the modified effective viscosity. The variation of the injection parameter (s) is shown in Figure 6. Increasing s corresponds to a reduction in the strength of injection and, consequently, less fluid is introduced into the boundary layer, resulting in a reduction in the velocity near the stretching surface. The reduction is more pronounced for the aggregation case, where the higher effective viscosity increases the resistance to shear and further restricts momentum transport.

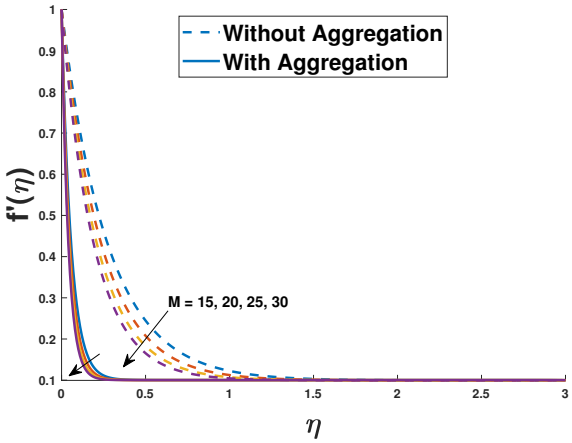


Figure 5. Effect of M on $f'(\eta)$ for $\phi_1 = \phi_2 = 0.05$, $A = 0.1$, $s = -1$, $\Gamma = 0.1$, and $Ec = 0.1$.

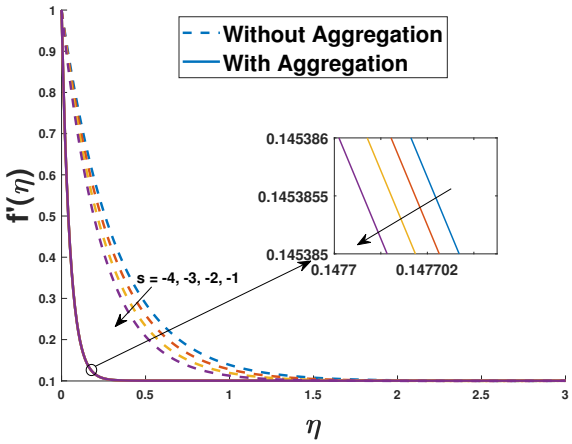


Figure 6. Effect of s on $f'(\eta)$ for $\phi_1 = \phi_2 = 0.05$, $A = 0.1$, $\Gamma = 0.1$, $Ec = 0.1$, and $M = 20$.

4.2. Effect of different parameters on thermal profile

The baseline parameter values used for the temperature profile analysis are $\phi_1 = \phi_2 = 0.05$, $A = 2$, $s = -1$, $\Gamma = 0.1$, $Ec = 0.1$, and $M = 20$. The influence of the velocity ratio parameter (A) on the temperature profile ($\theta(\eta)$) is shown in Figure 7. For the non-aggregation case, the temperature profile increases with A, whereas for the aggregation case, the temperature decreases as A increases. This difference arises from the modified thermal transport characteristics of the aggregated hybrid nanofluid. In particular, aggregation changes the effective thermophysical properties appearing in the energy equation and alters the velocity field that governs convective transport. Consequently, the increase in the external flow velocity associated with larger A produces different balances between convective and conductive heat transport in the two cases. For the non-aggregation fluid, this balance results in an increase in temperature, while for the aggregated fluid, the modified transport properties cause the convective effect associated with increasing A to promote greater removal of thermal energy from the near surface region, resulting in a decrease in temperature. The aggregation profiles therefore remain distinct from the non-aggregation profiles throughout the range of A considered.

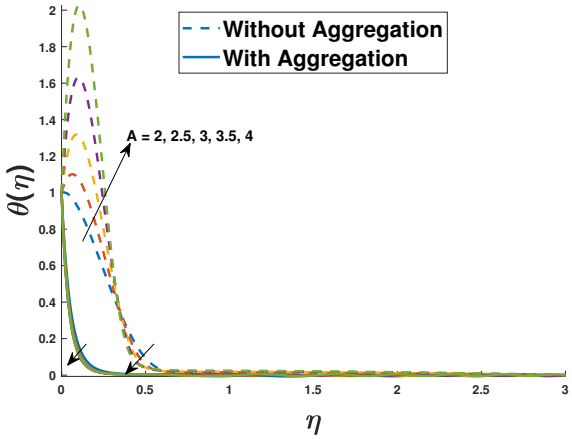


Figure 7. Effect of A on $\theta(\eta)$ for $\phi_1 = \phi_2 = 0.05$, $s = -1$, $\Gamma = 0.1$, $Ec = 0.1$, and $M = 20$.

Figure 8 illustrates the effect of injection parameter (s) on the temperature profile. For the non-aggregation case, increasing s, which corresponds to weaker injection for the negative values considered, reduces the temperature and modifies the thermal boundary layer through the altered fluid transport near the surface. Interestingly, the aggregated case exhibits an opposite variation, with the temperature increasing as s increases. This contrasting response indicates that the modified thermophysical properties associated with aggregation alter the balance between convective and conductive heat transport. Nevertheless, the temperature profile for the aggregation case remains below that of the non-aggregation case over the parameter range considered, indicating that the enhanced thermal transport associated with the aggregated nanoparticles remains influential in the overall thermal field.

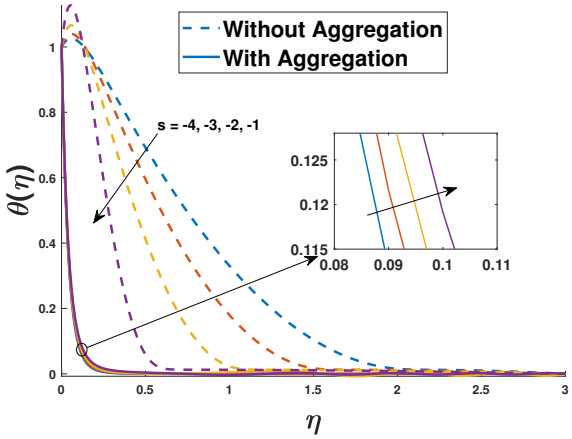


Figure 8. Effect of s on $\theta(\eta)$ for $\phi_1 = \phi_2 = 0.05$, $A = 2$, $\Gamma = 0.1$, $Ec = 0.1$, and $M = 20$.

The influence of the Eckert number (Ec) on the temperature profile is presented in Figure 9. Increasing Ec raises the temperature in aggregation and non-aggregation cases. This behavior is directly related to the viscous dissipation contribution in the energy equation. A larger Ec strengthens this contribution, corresponding to greater conversion of mechanical energy into internal thermal energy and consequently increasing the fluid temperature. The aggregation and non-aggregation

profiles retain their distinct thermal responses throughout the considered range, with the aggregation case exhibiting a lower temperature profile. The effect of the porosity parameter (Γ) on the temperature profile is shown in Figure 10. A slight increase in temperature is observed as Γ increases in both cases. This behavior is associated with the explicit appearance of Γ in the viscous dissipation term of the energy equation, through which an increase in Γ enhances the contribution of viscous dissipation to thermal energy generation. Furthermore, increasing Γ strengthens the porous medium resistance and consequently modifies the velocity field. The observed temperature response therefore reflects the combined effects of enhanced viscous dissipation and the associated change in fluid motion. The aggregation case remains at a lower temperature, consistent with the modified thermal transport properties of the aggregated hybrid nanofluid.

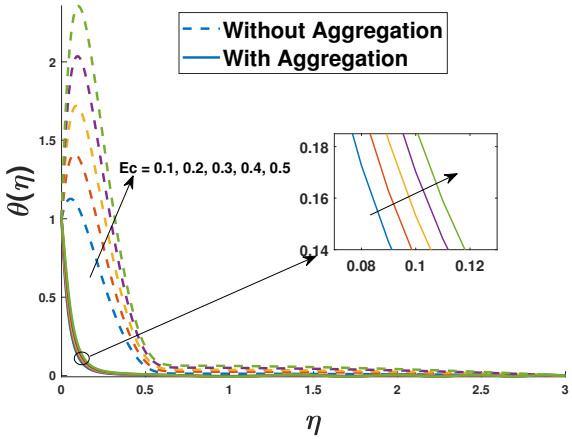


Figure 9. Effect of Ec on $\theta(\eta)$ for $\phi_1 = \phi_2 = 0.05$, $A = 2$, $s = -1$, $\Gamma = 0.1$, and $M = 20$.

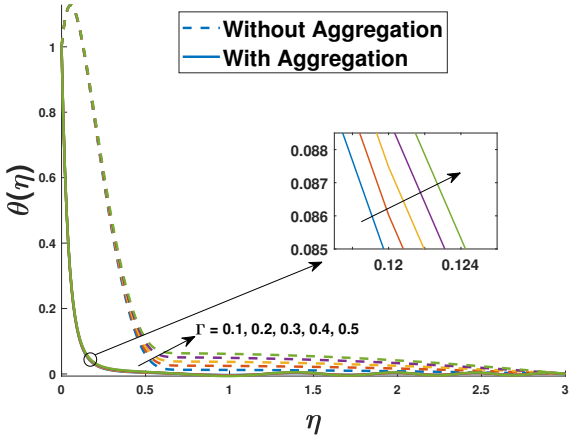
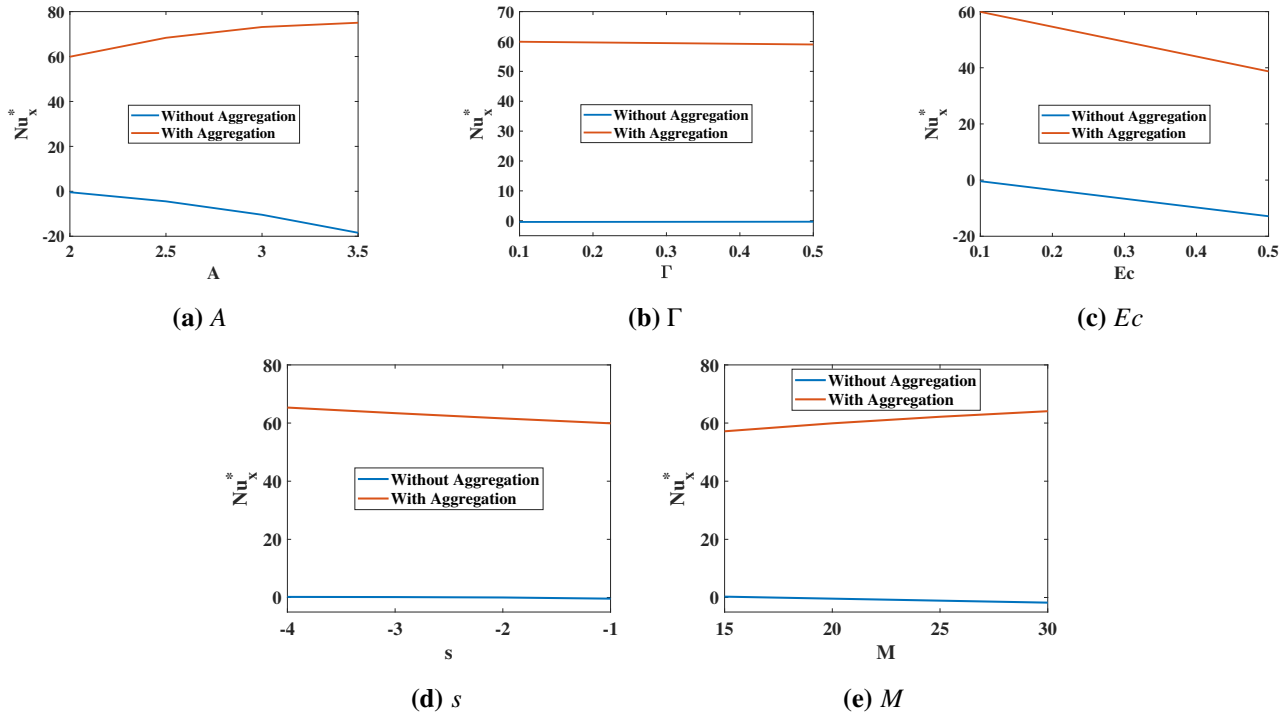


Figure 10. Effect of Γ on $\theta(\eta)$ for $\phi_1 = \phi_2 = 0.05$, $A = 2$, $s = -1$, $Ec = 0.1$, and $M = 20$.

The influence of aggregation on the flow and thermal fields arises from the simultaneous modification of the effective viscosity and thermal conductivity. The increase in effective viscosity associated with aggregation enhances the resistance to fluid motion, whereas the corresponding change in effective thermal conductivity modifies the thermal transport within the suspension. These effects

act through different transport mechanisms and therefore contribute jointly to the resulting velocity and temperature distributions.

The variation of the different parameters involved in the study on the local Nusselt number is demonstrated in Figure 11. The results indicate that the local Nusselt number is enhanced for all the parameters for the aggregation case because aggregation increases the hybrid nanofluid's effective thermal conductivity. Larger and more effective thermal-conducting pathways are produced within the fluid as nanoparticles aggregate. In comparison to the non-aggregation case, these structures improve internal energy transport and reduce thermal resistance near the surface, raising the heat transfer rate.



(a) A **(b)** Γ **(c)** Ec

(d) s **(e)** M

Figure 11. Effect of different parameters on the local Nusselt number.

5. Response surface methodology (RSM)

RSM is employed in this study to determine the optimal behavior of the local Nusselt number (Nu_x^*) for cases of aggregation and without aggregation under the influence of three key physical parameters: the total volume fraction of the nanoparticles (ϕ), the porosity parameter (Γ), and the magnetic parameter (M). This method enables a systematic investigation of the combined effects of these parameters and helps determine the appropriate parameter conditions required to maximize the heat transport efficiency of the fluid model. The essential step in this method is to characterize the dependence of the response function on the input factor variables, thereby identifying the most effective path toward the optimum point. In this study, a face-centered central composite design is used to explore this relationship between the response and input parameters. The input parameters, ϕ, Γ, and M are coded as A, B, and C, respectively; while the responses, which are Nu_x^* (without aggregation) and Nu_x^* (with aggregation), are coded as R1 and R2, respectively. The levels associated with the input variables used in the response analysis are presented in Table 5, whereas Table 6 reports the

20 experimental runs comprising the corresponding input and response values. These include 8 cube points, 6 axial points, and 6 central points. The quadratic model is expressed in Eq (5.1), comprising linear, quadratic, and two-way interaction terms, while three-way interaction terms are not included.

$$\text{Response} = \gamma_0 + \gamma_1 A + \gamma_2 B + \gamma_3 C + \gamma_{11} A^2 + \gamma_{22} B^2 + \gamma_{33} C^2 + \gamma_{12} AB + \gamma_{23} BC + \gamma_{13} AC, \tag{5.1}$$

where γ_i $(i = 0, 1, 2, 3)$ represent the coefficients of the linear terms, γ_{ii} $(i = 1, 2, 3)$ represent the coefficients of the quadratic terms, and γ_{ij} $(i < j; i, j = 1, 2, 3)$ represent the coefficients of the interaction terms.

Table 5. Parameter codes with their corresponding levels.

Parameters	**Codes**	**Level**		
		Low(-1)	**Middle(0)**	**High(1)**
ϕ	A	0.01	0.055	0.1
Γ	B	0.1	0.3	0.5
M	C	10	15	20

Table 6. Data set showing coded and response values.

Coded values			**Responses**	
A	**B**	**C**	**R1**	**R2**
-1	-1	-1	1.17406	14.18464
1	-1	-1	1.18717	16.14691
-1	1	-1	1.21004	13.87978
1	1	-1	1.24448	15.89266
-1	-1	1	0.53410	14.35065
1	-1	1	0.14003	17.09650
-1	1	1	0.56971	14.01439
1	1	1	0.19522	16.90432
-1	0	0	0.86528	14.14745
1	0	0	0.67913	16.58889
0	-1	0	0.77682	15.44319
0	1	0	0.82235	15.16085
0	0	-1	1.22109	14.97056
0	0	1	0.39970	15.51679
0	0	0	0.80035	15.30113
0	0	0	0.80035	15.30113
0	0	0	0.80035	15.30113
0	0	0	0.80035	15.30113
0	0	0	0.80035	15.30113
0	0	0	0.80035	15.30113

The RSM analysis is carried out using the 20 data sets listed in Table 6, and the corresponding results are obtained as follows:

$$R1 = 1.8184 + 6.136A + 0.0977B - 0.07114C - 13.83A^2 - 0.0157B^2 + 0.000407C^2 + 0.568AB - 0.45340AC - 0.00031BC, \quad (5.2)$$

$$R2 = 13.5863 + 8.549A - 0.889B + 0.0745C + 32.59A^2 - 0.004B^2 - 0.002340C^2 + 2.704AB + 0.9226AC + 0.00383BC. \quad (5.3)$$

Tables 7 and 8 depict the analysis of variance (ANOVA) results for the corresponding factors together with their p-values. Based on these results, the factors with p-values less than 0.05 are considered statistically significant, whereas those with p-values greater than 0.05 are treated as insignificant and disregarded from the regression model. Hence, upon eliminating the insignificant terms from Eqs (5.2) and (5.3), the resulting expressions are written as

$$R1 = 1.8184 + 6.136A + 0.0977B - 0.07114C - 13.83A^2 + 0.000407C^2 + 0.568AB - 0.45340AC, \quad (5.4)$$

$$R2 = 13.5863 + 8.549A - 0.889B + 0.0745C + 32.59A^2 - 0.002340C^2 + 2.704AB + 0.9226AC. \quad (5.5)$$

Table 7. Analysis of variance for local Nusselt number (without aggregation).

Source	DF	P-value	Adj MS	F-Value	Adj SS	Remarks
Error	10		0.00002		0.00022	
Lack-of-Fit	5	*	0.00004	*	0.00022	
Pure Error	5		0.0000		0.0000	
Total	19				1.93646	
Model	9	< 0.001	0.21514	9685.65	1.93624	Significant
Square	3	< 0.001	0.61666	27762.37	0.00280	
A*A	1	< 0.001	0.08229	3704.96	0.00216	
B*B	1	0.829	0.00527	237.37	0.0000	
C*C	1	0.005	1.76241	79344.77	0.00028	
Linear	3	< 0.001	0.00093	42.02	1.84997	
A	1	< 0.001	0.00216	97.15	0.08229	
B	1	< 0.001	0.0000	0.05	0.00527	
C	1	< 0.001	0.00028	12.82	1.76241	
2-Way Interaction	3	< 0.001	0.02782	1252.56	0.08347	
A*B	1	0.012	0.00021	9.42	0.00021	
A*C	1	< 0.001	0.08326	3748.22	0.08326	
B*C	1	0.856	0.0000	0.03	0.0000	

$R^2 = 99.99\%$ Adjusted $R^2 = 99.98\%$ Predicted $R^2 = 99.91\%$

RMSE = 0.0047130

The fitted model for the local Nusselt number (without aggregation) produces an F-value of 9685.65 with $p < 0.05$, whereas the model for the local Nusselt number (with aggregation) shows an F-value of

9348.13 with $p < 0.05$. This shows that both models are statistically highly significant. The regression coefficient R^2 for both models is 99.99%, indicating a high level of fitting accuracy. It should be noted that the response values used in the RSM analysis are obtained from deterministic FEM simulations rather than physical experiments. Consequently, the numerical responses contain no experimental measurement noise, and the residual variation associated with the fitted response surface can be very small. This can result in relatively large F-values and correspondingly high R^2 values, as observed in Tables 7 and 8. The high F-values therefore reflect the close agreement between the quadratic response surface models and the numerical FEM data.

Table 8. Analysis of variance for local Nusselt number (with aggregation).

Source	DF	P-Value	Adj MS	F-Value	Adj SS	Remarks
Error	10		0.0002		0.0019	
Lack-of-Fit	5	*	0.0004	*	0.0019	
Pure Error	5		0.0000		0.0000	
Total	19				15.8693	
Model	9	< 0.001	1.7630	9348.13	15.8674	Significant
Square	3	< 0.001	5.1674	27398.77	0.0157	
A*A	1	< 0.001	14.5259	77020.24	0.0120	
B*B	1	0.986	0.1877	995.01	0.0000	
C*C	1	< 0.001	0.7885	4151.05	0.0094	
Linear	3	< 0.001	0.0052	27.77	15.5021	
A	1	< 0.001	0.0120	63.50	14.5259	
B	1	< 0.001	0.0000	0.00	0.1877	
C	1	< 0.001	0.0094	49.89	0.7885	
2-Way Interaction	3	< 0.001	0.1165	617.84	0.3496	
A*B	1	0.001	0.0047	25.15	0.0047	
A*C	1	< 0.001	0.3447	1827.76	0.3447	
B*C	1	0.448	0.0001	0.62	0.0001	
R^2 = 99.99%	Adjusted R^2 = 99.98%		Predicted R^2 = 99.80%			
	RMSE = 0.0137331					

Figures 12 and 13 display the residual plots for both models. Each figure contains the normal probability plot, residual versus fits plot, histogram of residuals, and residuals versus order plot. The normal probability plots for both models indicate that the residuals are nearly aligned along a straight line, implying that the errors are normally distributed. The residuals versus fitted value plots indicate that the residuals are scattered on both sides of the zero reference line for both models. No systematic pattern or dependence on the predicted values is observed, indicating a stable error variance and reliable model fitting. The histogram of residuals for both models exhibit a bell-shaped pattern, suggesting that the residuals follow an approximately normal distribution. The residuals versus order plots reveal no systematic pattern or continuous increasing or decreasing trends across the sequence of observations. This suggests that the residuals are independent, with no evidence of serial correlation in the data. Therefore, the residual diagnostics indicate that the fundamental assumptions of regression analysis are satisfactorily fulfilled, which supports the reliability of the developed regression models.

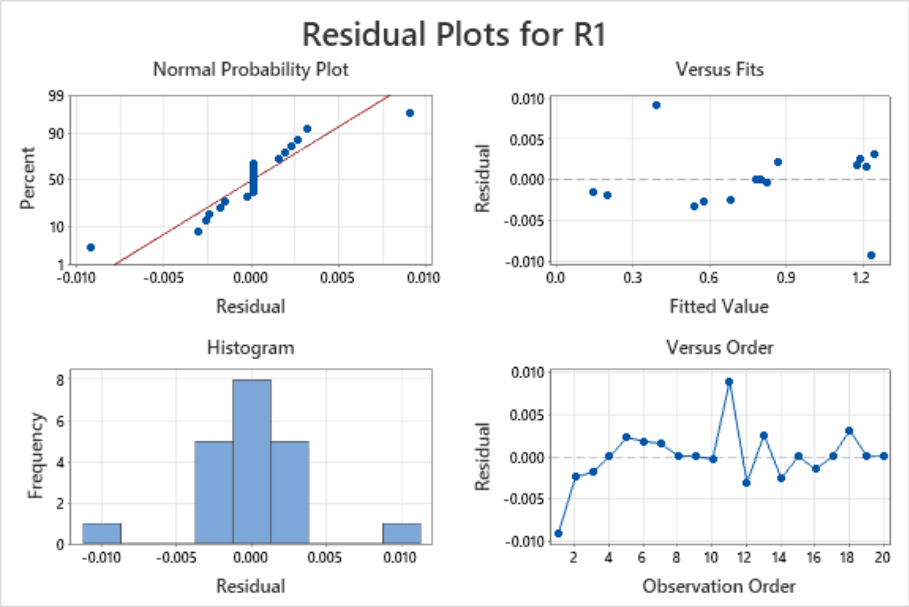


Figure 12. Residual plots for the local nusselt number without aggregation (R1).

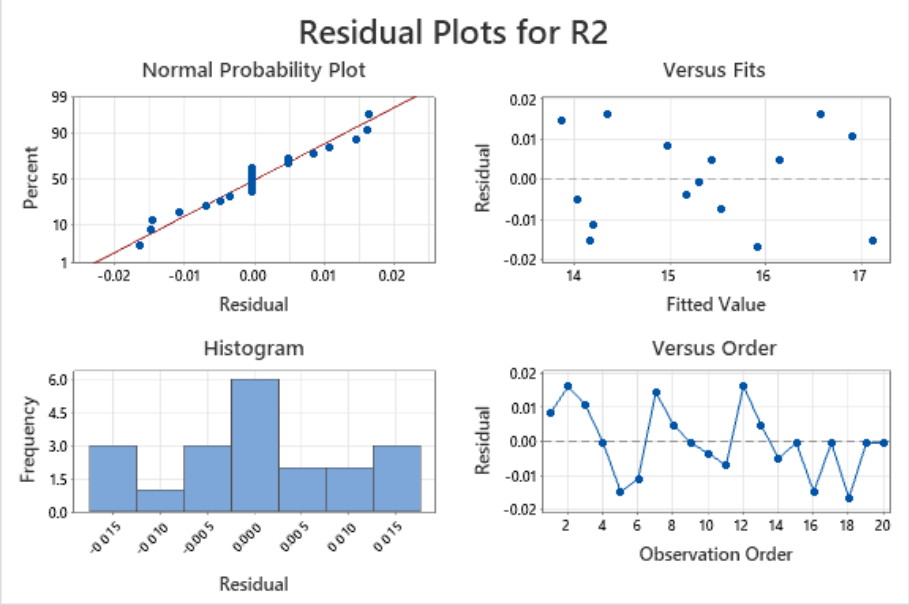
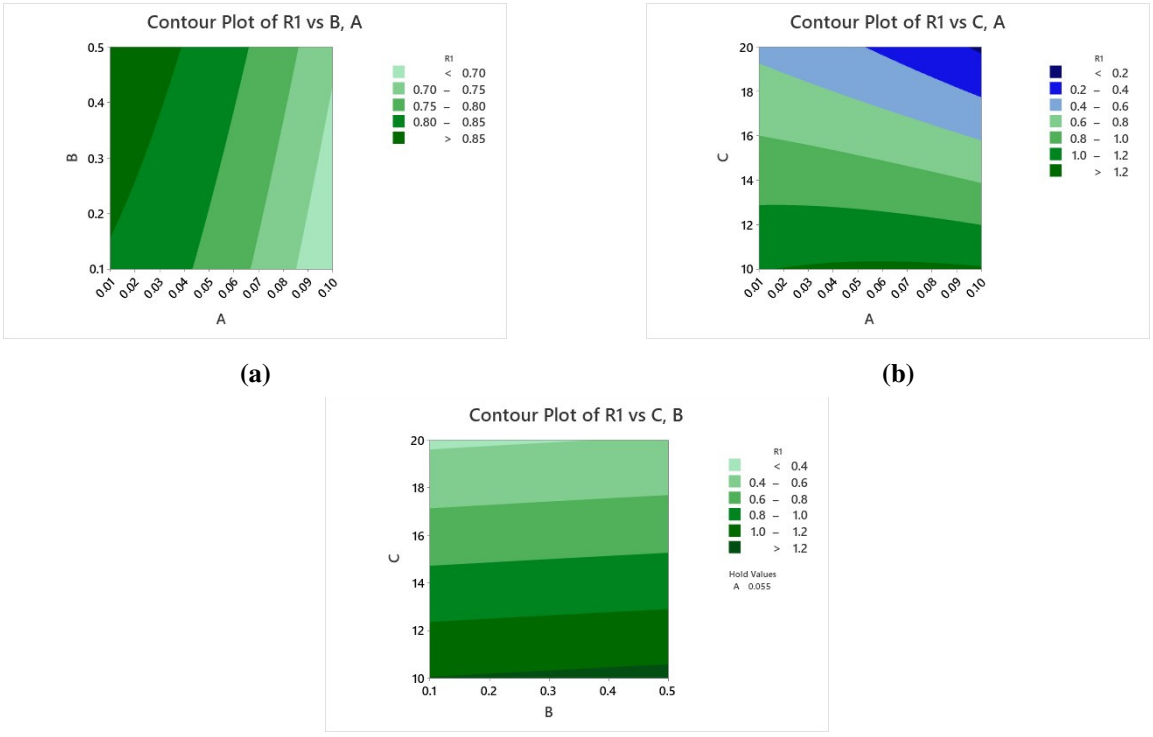


Figure 13. Residual plots for the local nusselt number with aggregation (R2).

Figures 14–17 illustrate the interdependent effects between the input variables, namely, the total volume fraction (ϕ), the porosity parameter (Γ), and the magnetic parameter (M); and the two response variables: the local Nusselt number without aggregation (R1) and the local Nusselt number with aggregation (R2). It can be observed from Figures 14(a) and 15(a) that at the mid-level of factor C, response R1 attains higher values when factor A is at its lower level and factor B is at its higher values. This suggests that lower nanoparticle volume fraction together with higher porosity of the medium leads to an augmentation in the heat transport capability when aggregation effects are not considered.

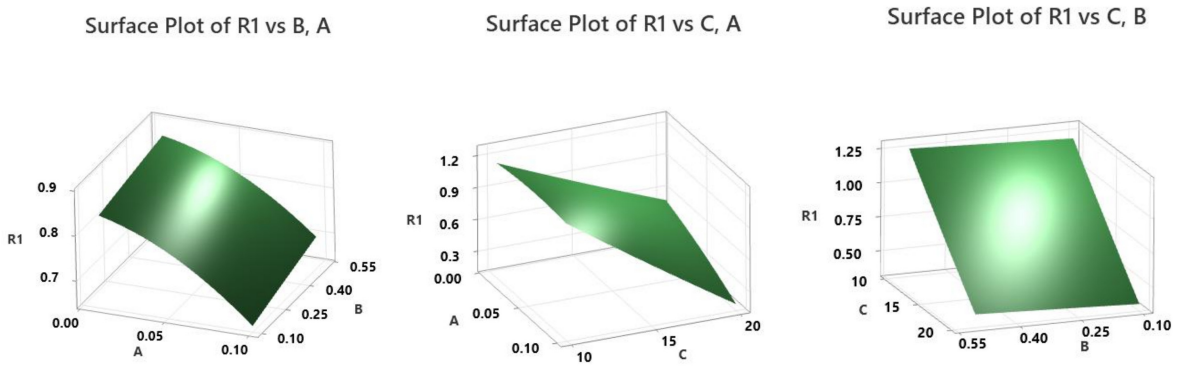
Figures 14(b) and 15(b) show that at the mid-level of factor B, response function R1 decreases with increasing values of factors A and C, whereas lower values of factor C lead to an increase in R1. Figures 14(c) and 15(c) indicate that for the mid-level of factor A, response R1 increases at lower values of factor C and at moderate to higher values of factor B, suggesting that weaker magnetic effects and higher porosity of the medium leads to improvement in the heat transport capability in the system in the absence of aggregation.



(a) **(b)**

(c)

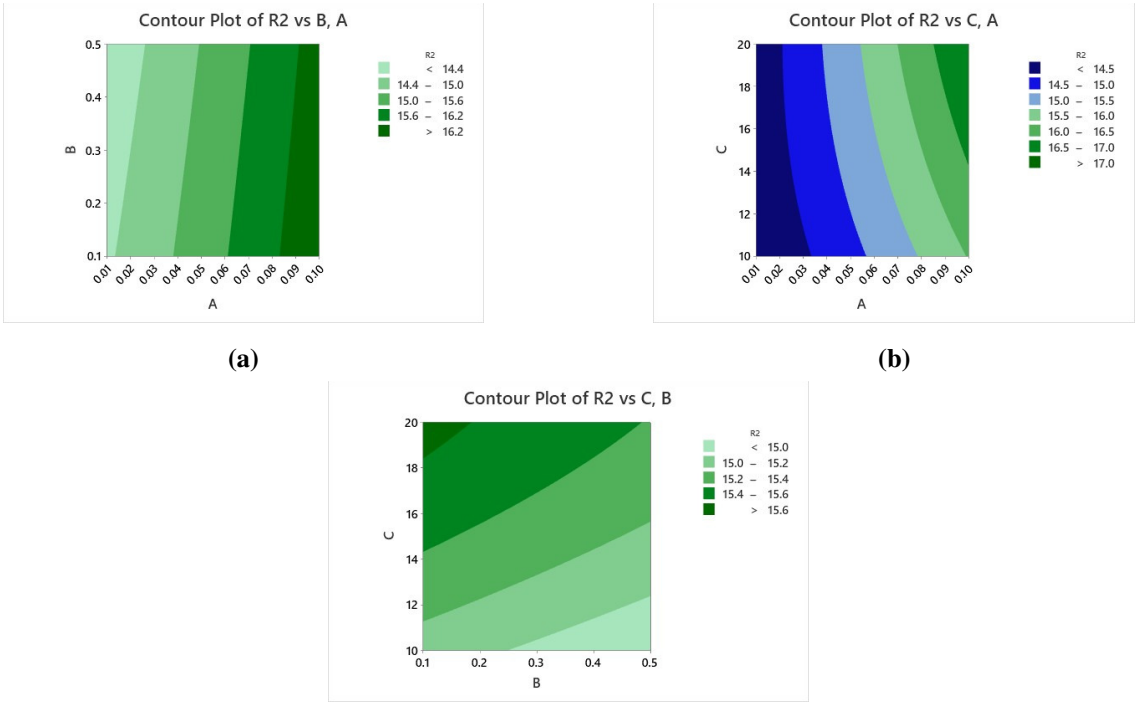
Figure 14. Contour plots for local Nusselt number (without aggregation).



(a) **(b)** **(c)**

Figure 15. Surface plots for local Nusselt number (without aggregation).

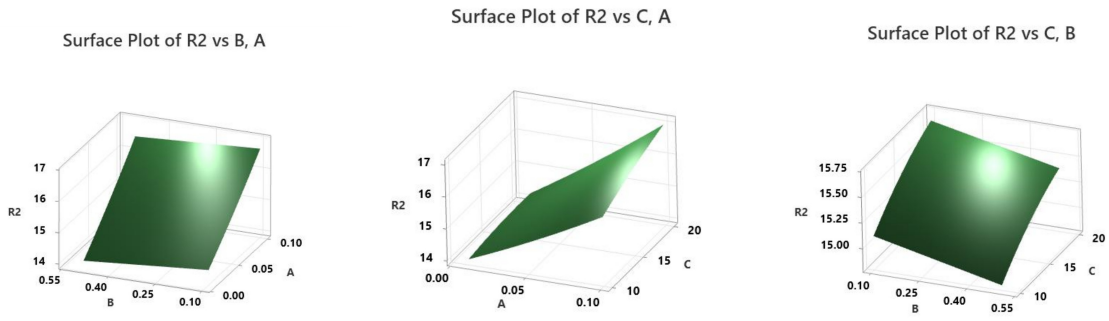
The interaction between factors A and B on the response function R2 at the mid-level of factor C is depicted in Figures 16(a) and 17(a). It is observed that augmenting the value of factor A leads to a rise in response R2, regardless of the range of factor B. This indicates that higher particle volume fractions lead to an advancement in the heat transport capability when aggregation effects are considered. Figures 16(b) and 17(b) show that lower values of factor A leads to an abrupt reduction in response R2 for all levels of factor C. However, at higher values of factors A and C, the response function R2 attains a high value. This behavior suggests that low particle volume fraction leads to reduced aggregation of nanoparticles, which consequently diminishes the enhancement in heat transport. It can be observed from Figures 16(c) and 17(c) that at the mid-level of factor A, response R2 is increased for lower values of factor B and higher values of factor C.



(a) **(b)**

(c)

Figure 16. Contour plots for local Nusselt number (with aggregation).



(a) **(b)** **(c)**

Figure 17. Surface plots for local Nusselt number (with aggregation).

The response surface analysis further identifies the parameter region associated with enhanced heat transfer for the aggregated case. As shown in Table 9, the response optimizer predicts a maximum Nu_x^* of 17.1113 at $\phi = 0.1$, $\Gamma = 0.1$, and $M = 20$, with a composite desirability of 1. The surface plots in Figure 17 are consistent with this result, with higher values of Nu_x^* occurring toward $\phi = 0.1$, $\Gamma = 0.1$, and $M = 20$. For the interaction between ϕ and Γ, the response increases as ϕ increases from 0.05 to 0.1, with higher responses observed toward the lower values of Γ. For the $\phi - M$ interaction, the response increases toward $\phi = 0.1$ and $M = 20$. Similarly, the $\Gamma - M$ interaction shows higher values of Nu_x^* near $\Gamma = 0.1$ and $M = 20$, while increasing Γ is associated with a reduction in the response R2. Overall, the RSM results indicate that enhanced heat transfer is associated with the region centered around $\phi = 0.1$, $\Gamma = 0.1$, and $M = 20$.

Table 9. Optimized parameter combination and predicted response for the aggregated case.

Parameter	**Optimized value**
ϕ	0.1
Γ	0.1
M	20
Predicted Nu_x^*	17.1113
Composite desirability	1.000

To verify the optimum condition identified by the RSM analysis, an additional FEM calculation is performed using the optimized parameter combination, $\phi = 0.1$, $\Gamma = 0.1$, and $M = 20$, while keeping the remaining parameters unchanged. As shown in Table 9, the RSM model predicts a local Nusselt number (with aggregation) of 17.1113, whereas the independent FEM calculation yields $Nu_x^* = 17.0965$. The absolute difference between the RSM prediction and the FEM result is 0.0148, corresponding to a percentage difference of only 0.0866%. The close agreement between the two results confirms that the RSM model provides a reliable prediction of the heat transfer response at the identified optimum.

6. Sensitivity analysis

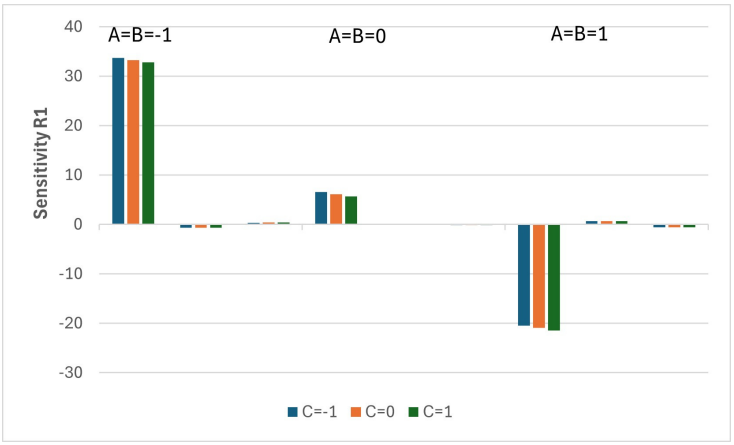
To quantify how variations in the input variables influence the response variables, sensitivity analysis is employed. Sensitivity analysis is an important tool for analyzing how variations in input parameters influence the outputs, and it assists researchers in identifying the most suitable combination of parameters for achieving optimal system performance. In this study, we perform a sensitivity analysis of the local Nusselt number (Nu_x^*) for aggregation and non-aggregation cases under varying input parameters. The sensitivity analysis is expressed in terms of the partial derivatives of the responses, where the response variables R1 and R2 are evaluated with respect to the governing factors A, B, and C. Thus, for each response, the sensitivity coefficients with respect to A, B, and C are defined as

$$S_A^{R1} = \frac{\partial R1}{\partial A} = 6.136 - 27.66A + 0.568B - 0.4534C,$$
$$S_B^{R1} = \frac{\partial R1}{\partial B} = 0.568A + 0.0977B,$$

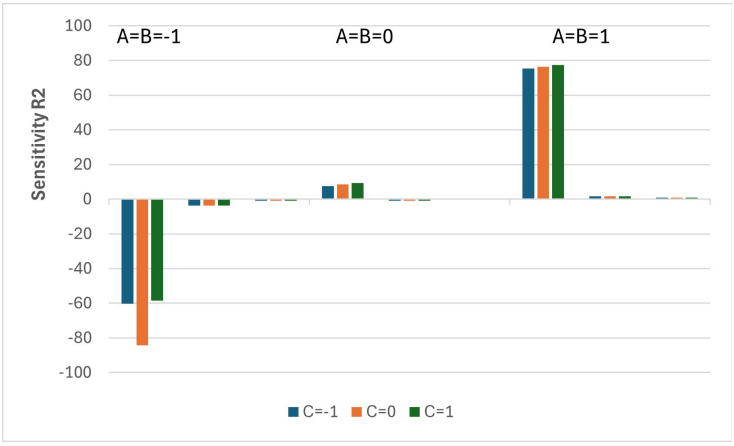
$$S_C^{R1} = \frac{\partial R1}{\partial C} = -0.07114 - 0.4534A + 0.000814C,$$
$$S_A^{R2} = \frac{\partial R2}{\partial A} = 8.549 + 65.18A + 2.704B + 0.9226C,$$
$$S_B^{R2} = \frac{\partial R2}{\partial B} = -0.889 + 2.704A,$$
$$S_C^{R2} = \frac{\partial R2}{\partial C} = 0.0745 + 0.9226A - 0.00468C.$$

These equations are unnormalized local sensitivity measures, as they are obtained directly from the derivatives of the regression equations without scaling by the response of the corresponding parameter. A positive sensitivity coefficient indicates that an increase in the corresponding parameter locally increases the response, whereas a negative value indicates a local decrease. The magnitude of the coefficient represents the rate of change of the response with respect to the corresponding parameter.

Figure 18 shows the sensitivity of the local Nusselt number without aggregation (R1) and with aggregation (R2) with respect to input parameters, volume fraction of nanoparticles (A), porosity parameter (B), and magnetic parameter (C).



(a)



(b)

Figure 18. Sensitivity analysis plots of (a) R1 and (b) R2.

For the analysis, the parameter combinations $A = B = -1$, $A = B = 0$, and $A = B = 1$ are treated as reference scenarios, while parameter C is varied at the levels -1, 0, and 1. Figure 18(a) illustrates that the sensitivity of parameter A with respect to R1 is highest when $A = B = -1$. When $A = B = 0$, all parameters exhibit lower sensitivity to R1, with B and C showing almost negligible influence. On the other hand, parameter A exhibits negative sensitivity to R1 when A=B=1, while B and C continue to show weak sensitivity to R1. Figure 18(b) demonstrates that parameter A shows highest sensitivity toward R2 when $A = B = 1$, whereas a negative sensitivity is observed when $A = B = -1$. The other parameters show very low sensitivity to R2 as A and B vary from -1 to 1.

7. Conclusions

In this study, we principally investigate the MHD stagnation point flow of TiO_2-Al_2O_3/EG nanofluid over a stretching sheet within a porous medium, accounting for the influence of viscous dissipation and nanoparticle aggregation. The Krieger-Dougherty model is suitably modified to formulate the effective viscosity of the hybrid nanofluid, while the Maxwell and Bruggeman models are modified to accommodate its aggregation-dependent thermal properties. We employ RSM to examine the interaction of the total particle volume fraction with the heat transfer capability of the hybrid nanofluid, considering cases with and without aggregation of nanoparticles. Sensitivity analysis is concurrently employed to determine the input parameters having the greatest influence on the responses. The principal results of the study are outlined below:

- The heat transfer performance of the hybrid nanofluid is noticeably enhanced when nanoparticle aggregation is taken into account compared to the case without aggregation effects.
- The velocity profiles indicate that nanoparticle aggregation leads to the reduction in fluid velocity due to increased effective viscosity of the hybrid nanofluid, which enhances resistance to fluid motion.
- The temperature profiles indicate that fluid temperature is lowered in the aggregation case as aggregation increases the thermal conductivity of the fluid accelerating heat diffusion from the surface.
- The applied magnetic field indirectly enhances thermal transport in the hybrid nanofluid when aggregation of nanoparticles are taken in account.
- Augmenting the Eckert number elevates the fluid temperature, as viscous dissipation facilitates the conversion of kinetic energy to internal thermal energy.
- The RSM analysis reveals that, in the presence of nanoparticle aggregation effects, increasing the nanoparticle volume fraction enhances the heat transfer performance, whereas lower nanoparticle concentrations lead to a reduction in the heat transfer capability.
- In the absence of nanoparticle aggregation effects, the analysis reveals the heat transfer enhancement is more pronounced at lower particle volume fractions together with higher values of the porosity parameter.
- The sensitivity analysis reveals that the nanoparticle volume fraction exerts the strongest influence on the local Nusselt number in the presence of nanoparticle aggregation, particularly when combined with higher levels of the porosity and magnetic parameters. In contrast, the porosity and magnetic parameters exhibit comparatively weaker effects on the heat transfer performance across all considered ranges of the volume fraction and the porosity parameter variations.

- The optimum condition identified by the RSM for enhanced heat transfer in the presence of nanoparticle aggregation shows close agreement with the corresponding FEM calculation, with a percentage difference of only 0.0866%.

8. Future research directions

This study can be extended in several directions. In future work, researchers may consider more complex hybrid nanofluids, such as ternary or higher order hybrid nanofluids, together with different nanoparticle aggregation mechanisms and aggregate structures. The effects of additional physical phenomena, including non-Newtonian fluid behavior, velocity slip, non-uniform magnetic fields, and variable thermal conditions, may also be investigated. Furthermore, the response surface and sensitivity analyzes can be extended by incorporating a wider range of governing parameters and flow configurations. Experimental investigation would also be valuable for validating the proposed aggregation model and assessing its applicability to practical heat transfer systems. Such extensions could provide further insight into the thermal performance and optimization of aggregated hybrid nanofluids in engineering applications.

Author contributions

Jeremy Rymbai and Rajesh Sharma: Conceptualization, Methodology, Software, Validation, Formal analysis, Investigation, Visualization; Jeremy Rymbai: Writing–original draft; Rajesh Sharma: Supervision, Project administration, Resources, Writing–review & editing; Anuar Ishak: Methodology, Validation, Formal analysis, Writing–review & editing. All authors have read and approved the final version of the manuscript for publication.

Use of Generative-AI tools declaration

The authors declare they have not used Artificial Intelligence (AI) tools in the creation of this article.

Acknowledgments

The authors would like to acknowledge Universiti Kebangsaan Malaysia for financial support under grant number GP-K017380, and North-Eastern Hill University, Shillong, India for providing the necessary research facilities.

Conflict of interest

The authors declare no conflicts of interest.

References

1. J. Sarkar, P. Ghosh, A. Adil, A review on hybrid nanofluids: recent research, development and applications, *Renew. Sust. Energy Rev.*, **43** (2015), 164–177. https://doi.org/10.1016/j.rser.2014.11.023

2. S. Khalatbari, P. Jalili, B. Jalili, D. D. Ganji, Investigating the improvement of heat transfer and flow characteristics of hybrid nanofluids: a comprehensive review, In: *Proceedings of the Institution of Mechanical Engineers, Part E: Journal of Process Mechanical Engineering*, **240** (2026), 5932–5947. https://doi.org/10.1177/09544089251318785

3. N. A. C. Sidik, H. A. Mohammed, O. A. Alawi, S. Samion, A review on preparation methods and challenges of nanofluids, *Int. Commun. Heat Mass Transfer*, **54** (2014), 115–125. https://doi.org/10.1016/j.icheatmasstransfer.2014.03.002

4. J. Mackolil, B. Mahanthesh, Sensitivity analysis of Marangoni convection in TiO_2-EG nanoliquid with nanoparticle aggregation and temperature-dependent surface tension, *J. Thermal Anal. Calorim.*, **143** (2021), 2085–2098. https://doi.org/10.1007/s10973-020-09642-7

5. A. Nikulin, A. S. Moita, A. L. N. Moreira, S. M. S. Murshed, A. Huminic, Y. Grosu, et al., Effect of Al_2O_3 nanoparticles on laminar, transient and turbulent flow of isopropyl alcohol, *Int. J. Heat Mass Transfer*, **130** (2019), 1032–1044. https://doi.org/10.1016/j.ijheatmasstransfer.2018.10.114

6. W. Ajeeb, R. R. S. T. Silva, S. M. S. Murshed, Experimental investigation of heat transfer performance of Al_2O_3 nanofluids in a compact plate heat exchanger, *Appl. Thermal Eng.*, **218** (2023), 119321. https://doi.org/10.1016/j.applthermaleng.2022.119321

7. S. Zainodin, A. Jamaludin, R. Nazar, I. Pop, MHD mixed convection flow of hybrid ferrofluid through stagnation-point over the nonlinearly moving surface with convective boundary condition, viscous dissipation, and joule heating effects, *Symmetry*, **15** (2023), 1–29. https://doi.org/10.3390/sym15040878

8. K. N. V. C. Bhargava, S. M. Ibrahim, R. Kodi, Magneto-hydrodynamic mixed convection chemically rotating and radiating 3D hybrid nanofluid flow through porous media over a stretched surface, *Math. Model. Numer. Simul. Appl.*, **4** (2024), 495–513. https://doi.org/10.53391/mmnsa.1438636

9. A. B. Vishalakshi, R. Mahesh, U. S. Mahabaleshwar, A. K. Rao, L. M. Pérez, D. Laroze, MHD hybrid nanofluid flow over a stretching/shrinking sheet with skin friction: effects of radiation and mass transpiration, *Magnetochemistry*, **9** (2023), 1–13. https://doi.org/10.3390/magnetochemistry9050118

10. A. Yusuf, M. M. Bhatti, R. Ellahi, M. Marin, Magnetized ternary hybrid nanofluid flow over a curved catalytic surface embedded in a porous medium with Beavers-Joseph slip, volumetric and surface nonthermal heating, *Discover Nano*, **21** (2026), 206. https://doi.org/10.1186/s11671-026-04625-3

11. P. K. Pattnaik, M. Shamshuddin, S. O. Salawu, S. Panda, U. Khan, Modelling the effects of particle shape and slip conditions on a buoyancy-driven rotating flow of hybrid nanofluid in a biaxially stretching sheet, *Int. J. Mech. Mater. Design*, **22** (2026), 44. https://doi.org/10.1007/s10999-025-09855-4

12. S. Pradeep, P. V. Kumar, Study of cross-diffusion effects on unsteady magnetohydrodynamic hybrid nanofluid flow over an inclined vertical plate, *Discover Nano*, **21** (2026), 199. https://doi.org/10.1186/s11671-026-04611-9

13. M. Awais, T. Salahuddin, R. M. Hafez, Z. Jastaneyah, H. Al Garalleh, M. O. Sidi, Mixed convection Carreau-Yasuda nanofluid flow with heat transfer analysis by Cattaneo-Christov heat and mass transfer models, *Comput. Biol. Med.*, **209** (2026), 111705. https://doi.org/10.1016/j.compbiomed.2026.111705
14. A. Abderrahmane, N. A. A. Qasem, O. Younis, R. Marzouki, A. Mourad, N. A. Shah, et al., MHD hybrid nanofluid mixed convection heat transfer and entropy generation in a 3-D triangular porous cavity with zigzag wall and rotating cylinder, *Mathematics*, **10** (2022), 1–18. https://doi.org/10.3390/math10050769
15. M. Z. Saghir, M. M. Rahman, Forced convection of Al_2O_3-Cu, TiO_2-SiO_2, FWCNT-Fe_3O_4, and ND-Fe_3O_4 hybrid nanofluid in porous media, *Energies*, **13** (2020), 1–19. https://doi.org/10.3390/en13112902
16. S. Hazarika, S. Ahmed, A. J. Chamkha, Analysis of platelet shape Al_2O_3 and TiO_2 on heat generative hydromagnetic nanofluids for the base fluid $C_2H_6O_2$ in a vertical channel of porous medium, *Walailak J. Sci. Tech.*, **18** (2021), 21424.
17. J. O. Oladetan, F. M. Fujah, O. S. Omosehin, E. O. Atofarati, U. Nwabuko, O. T. Olakoyejo, et al., Numerical investigation of heat transfer performance of hybrid nanofluid in porous substrate in microchannel heat sink, *Int. J. Appl. Comput. Math.*, **11** (2025), 151. https://doi.org/10.1007/s40819-025-01973-z
18. S. Taimir, S. Bibi, A. Ehsan, M. Awais, M. Khan, R. M. Hafez, et al., Numerical study of MHD natural convection flow inside a porous cavity with chemical reaction and Soret-Dufour effects, *Results Surfaces Interfaces*, **25** (2026), 100932. https://doi.org/10.1016/j.rsurfi.2026.100932
19. R. M. Hafez, A. Naeem, Z. Abbas, M. Y. Rafiq, Optimization and nonlinear thermal sensitivity analysis of Jeffrey fluid flow between permeable disks with modified Darcy law: implications for energy and cooling systems, *Case Stud. Thermal Eng.*, **81** (2026), 107975. https://doi.org/10.1016/j.csite.2026.107975
20. C. M. Mohana, R. M. Hafez, I. Touil, F. L. Rashid, M. Kezzar, R. K. Bangalore, et al., Thermal performance and flow characteristics of methanol based Fe_3O_4-$CoFe_2O_4$-Co_3O_4 nanofluid systems: numerical and ANN approaches, *Arab J. Basic Appl. Sci.*, **33** (2026), 445–465. https://doi.org/10.1080/25765299.2026.2719976
21. A. K. Al-Hadhrami, L. Elliot, D. B. Ingham, A new model for viscous dissipation in porous media across a range of permeability values, *Transp. Porous Media*, **53** (2003), 117–122. https://doi.org/10.1023/A:1023557332542
22. M. Motevasel, A. R. S. Nazar, M. Jamialahmadi, The effect of nanoparticles aggregation on the thermal conductivity of nanofluids at very low concentrations: experimental and theoretical evaluations, *Heat Mass Transfer*, **54** (2018), 125–133. https://doi.org/10.1007/s00231-017-2116-2
23. N. P. Karagiannakis, E. D. Skouras, V. N. Burganos, Modelling thermal conduction in nanoparticle aggregates in the presence of surfactants, *Nanomaterials*, **10** (2020), 1–21. https://doi.org/10.3390/nano10112288
24. H. Tahmooressi, A. Kasaeian, A. Tarokh, R. Razaei, M. Hoorfar, Numerical simulation of aggregation effect on nanofluids thermal conductivity using the lattice Boltzmann method, *Int. Commun. Heat Mass Transfer*, **110** (2020), 104408. https://doi.org/10.1016/j.icheatmasstransfer.2019.104408

25. P. Rana, W. Al-Kouz, B. Mahanthesh, J. Mackolil, Heat transfer of TiO_2-EG nanoliquid with active and passive control of nanoparticles subject to nonlinear Boussinesq approximation, *Int. Commun. Heat Mass Transfer*, **126** (2021), 105443. https://doi.org/10.1016/j.icheatmasstransfer.2021.105443

26. H. S. Chen, Y. L. Ding, Y. R. He, C. Q. Tan, Rheological behaviour of ethylene glycol based titania nanofluids, *Chem. Phys. Lett.*, **444** (2007), 333–337. https://doi.org/10.1016/j.cplett.2007.07.046

27. S. K. Rawat, M. Yaseen, A. Shafiq, M. Kumar, Q. M. Al-Mdallal, Nanoparticle aggregation effect on nonlinear convective nanofluid flow over a stretched surface with linear and exponential heat source/sink, *Int. J. Thermofluids*, **19** (2023), 100355. https://doi.org/10.1016/j.ijft.2023.100355

28. P. Rana, B. Mahanthesh, J. Mackolil, W. Al-Kouz, Nanofluid flow past a vertical plate with nanoparticle aggregation kinematics, thermal slip and significant buoyancy force effects using modified Buongiorno model, *Waves Random Complex Media*, **34** (2024), 3425–3449. https://doi.org/10.1080/17455030.2021.1977416

29. Z. Mahmood, U. Khan, Mixed convective flow of nanofluid across exponential surface: a numerical assessment of the impact of Darcy-Forchheimer and nanoparticle aggregation, *Numer. Heat Transfer Part A Appl.*, **86** (2025), 2192–2217. https://doi.org/10.1080/10407782.2023.2288265

30. I. Wole-Osho, E. C. Okonkwo, S. Abbasoglu, D. Kavaz, Nanofluids in solar thermal collectors: review and limitations, *Int. J. Thermophys.*, **41** (2020), 157. https://doi.org/10.1007/s10765-020-02737-1

31. S. P. Tembhare, D. P. Barai, B. A. Bhanvase, Performance evaluation of nanofluids in solar thermal and solar photovoltaic systems: a comprehensive review, *Renew. Sust. Energy Rev.*, **153** (2022), 111738. https://doi.org/10.1016/j.rser.2021.111738

32. J. A. Bocanegra, A. Marchitto, M. Misale, Nanofluids in solar collectors: a comprehensive review focused on its sedimentation, *Clean Technol. Environ. Policy*, **27** (2025), 1753–1784. https://doi.org/10.1007/s10098-024-02964-2

33. Q. Xiong, S. Altnji, T. Tayebi, M. Izadi, A. Hajjar, B Sundén, et al., A comprehensive review on the application of hybrid nanofluids in solar energy collectors, *Sustain. Energy Technol. Assess.*, **47** (2021), 101341. https://doi.org/10.1016/j.seta.2021.101341

34. A. Yusuf, M. M. Bhatti, R. Ellahi, Thermal and sensitivity analysis on regularized curved solar panels using non-Newtonian quaternary hybrid nanofluids: applications in solar collectors, *J. Indian Chem. Soc.*, **102** (2025), 102256. https://doi.org/10.1016/j.jics.2025.102256

35. M. Alktranee, Q. Al-Yasiri, M. A. Al-Furaiji, H. A. H. Al-Hamzawi, P. Bencs, M. Szabó, Performance improvement of flat plate solar collector employing phase change material bags and hybrid nanofluid, *Results Eng.*, **27** (2025), 106972. https://doi.org/10.1016/j.rineng.2025.106972

36. J. N. Reddy, *An introduction to the finite element method*, 3 Eds., New York: McGraw-Hill, 2006.

37. R. Sharma, A. Ishak, I. Pop, Dual solution of unsteady separated stagnation-point flow in a nanofluid with suction: a finite element analysis, *Indian J. Pure Appl. Phys.*, **55** (2017), 275–283.

38. S. R. Pop, I. Pop, T. Grosan, Radiation effects on the flow near the stagnation point of a stretching sheet, *Tech. Mech. Eur. J. Eng. Mech.*, **25** (2005), 100–106.

39. S. Masood, M. Farooq, A. Anjum, Influence of heat generation/absorption and stagnation point on polystyrene-TiO_2/H_2O hybrid nanofluid flow, *Sci. Rep.*, **11** (2021), 22381. https://doi.org/10.1038/s41598-021-01747-9

Appendix

Derivation of the viscous dissipation terms:
The viscous dissipation terms in Eq (2.3) are given by

$$\frac{\nu_{hnf}\varepsilon}{(C_p)_{hnf}k_p}u^2 + \frac{\nu_{hnf}}{(C_p)_{hnf}}\left(\frac{\partial u}{\partial y}\right)^2.$$

Using the transformation variables, $u = axf'(\eta)$ and $\eta = \sqrt{\frac{a}{\nu_f}}y$, the above equation reduces to

$$\frac{\nu_{hnf}\varepsilon}{(C_p)_{hnf}ak_p}\frac{a^2x^2}{(T_w - T_\infty)}f'^2 + \frac{\nu_{hnf}}{\nu_f(C_p)_{hnf}}\frac{a^2x^2}{(T_w - T_\infty)}f''^2.$$

Therefore, using the dimensionless quantities defined earlier, which are $\mathbb{A}_1 = \frac{\mu_{hnf}}{\mu_f}$, the Prandtl number: $Pr = \frac{(\mu C_p)_f}{k_f}$, the Eckert number: $Ec = \frac{u_w^2}{(C_p)_f(T_w - T_\infty)}$, and the porosity parameter: $\Gamma = \frac{\varepsilon\nu_f}{k_p a}$, the viscous dissipation term, which are obtained in Eq (3.2) can be expressed as

$$\mathbb{A}_1 Pr \cdot Ec(\Gamma f'^2 + f''^2).$$

AIMS Press

© 2026 the Author(s), licensee AIMS Press. This is an open access article distributed under the terms of the Creative Commons Attribution License (https://creativecommons.org/licenses/by/4.0)